# Macromodel-based simulation of membrane action in reinforced concrete structural members

Behrooz Yousefi, Mohammad Reza Esfahani & Mohammadreza Tavakkolizadeh

Published online: 11 Nov 2019.

Submit your article to this journal ☑

View related articles ☑

View Crossmark data ☑

Taylor & Francis
Taylor & Francis Group

Check for updates

# Macromodel-based simulation of membrane action in reinforced concrete structural members

Behrooz Yousefi [iD], Mohammad Reza Esfahani [iD], and Mohammadreza Tavakkolizadeh

Department of Civil Engineering, Ferdowsi University of Mashhad, Mashhad, Iran

**ABSTRACT**

This paper is devoted to present a two-stage fiber element-based method for studying the membrane action of RC structural members. The proposed method combines small and large displacement formulations through two separate stages. These stages include compressive arch action in small displacements and catenary stage in large displacements, separately. For structural problems with both geometric and material nonlinearity, the total Lagrangian and the updated Lagrangian formulations are taken into account to derive the governing equations. Also, the suggested method is able to consider the bond-slip behavior of reinforcing bars and shear deformations in the structural members. Finally, the accuracy of the authors' method is compared with the available experimental results and previous analytical methods in the literature. The results show that such a modeling method is capable of simulating compressive arch stage concurrently with the catenary action behavior.

## 1. Introduction

Accidental extreme events, such as imposed loads in the sudden loss of columns scenario, can apply abnormal loads to structures, which sequentially may suffer heavy damages, local failures or even collapse. A large number of researches have been examined and developed to study the progressive collapse behavior of RC frame structures (Sasani, Werner, and Kazemi 2011; Bao, Lew, and Kunnath 2014; Pham, Tan, and Yu 2017). In order to accomplish the simulation of material and geometrical nonlinearity, structural element models and relevant numerical procedures should aim at satisfying the accuracy, reliability, computational time, and robust algorithmic performance concurrently.

Based on the aforementioned aspects, some kinematic approaches are referred to as "lumped-plasticity" or "distributed-plasticity" models in the literature to account for material nonlinearities. The first element with concentrated plasticity comprises hinge model formulation and elastic section properties which is limited to axial, flexural and/or shear springs at the element ends (Franchi, Grierson, and Cohn 1981; Wu, Oehlers, and Griffith 2002; Kaewkulchai and Williamson 2004; Oehlers, Liu, and Seracino 2005; Izzuddin et al. 2008; Tsai and Lin 2008; Vlassis et al. 2008; Zhang, Lu, and Yin 2009; Parisi and Augenti 2012). The second element type, termed distributed-plasticity or fiber-based models, can essentially be classified as force-based

(FB) and displacement-based (DB) frame element. The FB frame element formulations stem from an equilibrium between a section and nodal forces which can be induced exactly in frame elements cases. The exact flexibility matrix can be computed for an arbitrary variation of the cross-section and constitutive law models (Valipour and Foster 2010; Li et al. 2011; Brunesi and Nascimbene 2014; Limkatanyu et al. 2014; Brunesi et al. 2015; Feng et al. 2016; Yu et al. 2017; Brunesi and Parisi 2017). However, in large displacement problems, the accuracy of the flexibility-based analysis depends on discretization, despite the fact that noticeable expansions have managed to reduce the mesh density (De Souza 2000). Discretization is required for field inconsistencies due to bending and membrane modes coupling to be moderated, which increases the computational cost significantly in highly geometrically nonlinear problems. Additionally, the adopted corotational transformation, implemented to exclude rigid body modes, can introduce important rotational limitations that can potentially lead to early analysis termination or prevent realistic results (Neuenhofer and Filippou 1998; Felippa and Haugen 2005). The vast majority of these formulations focused on elastic or hardening material responses, but only a few considered softening material behavior (e.g., Valipour and Foster (2010)). On the other hand, in a DB methodology, interpolations of transverse and axial frame element displacements are applied by a cubic and linear Hermitian polynomials, respectively, which are only approximations of the actual displacement fields in the presence of non-uniform beam cross-section with nonlinear material behavior (Bathe and Bolourchi 1979). Polynomial interpolation introduces field inconsistencies in this formulation, locking phenomena emerge, and even dense meshes are often practically insufficient to obtain accurate responses, or the convergence is carried out at a low speed (Alemdar and White 2005), or numerical instabilities (Gerasimidis et al. 2015). Several approaches have been proposed in the past to provide a mathematical formulation to cover these vulnerabilities (Kabeyasawa et al. 1983; Dvorkin, Onte, and Oliver 1988; Lodygowski and Szumigala 1992; Crivelli and Felippa 1993; Kara and Dundar 2010; Ben-Dor, Dubinsky, and Elperin 2009; Ghaisas et al. 2017; Bocciarelli and Barbieri 2017; Gharib, Vaziri, and Memarbashi 2019; Zhai, Wang, and Sun 2019). Moreover, the classical beam theory suffers from convergence failures and instabilities of the numerical solution algorithms in the presence of softening material such as concrete model. In addition, some specific failure modes, e.g., bond-slip and bar fracture, cannot be reflected.

In response to these challenges, research efforts from displacement-based to force-based standpoints have managed to significantly advance the efficacy of nonlinear analyses, proposing various structural element formulations and improved algorithms. Moreover, there are limited models which could cover the overall development of probable mechanisms, including the transition from compressive arch action (Yu and Tan 2014) to membrane action (Li et al. 2014), as well as their initial stiffness and ultimate capacities with increasing deformations. Therefore, the objective of this study is to present a two-stage formulation method for studying the RC compressive arch action in the first stage and RC membrane action in the second stage. Although the literature presents plenty of other interesting formulation approaches based on Timoshenko theory, there is still a lack of methods that consider the shear deformation effects concurrently with bond-slip behavior associated with the important attributes that affect the membrane action behavior of reinforced concrete (RC) structures, such as the material and geometric nonlinearities.

## 2. Stage 1: Kinematics of updated lagrangian in compressive arch action

At this stage, the formulation of the authors' scheme is presented. This new scheme can be applied for studying the compressive arch action in RC structures. It is able to consider the action of bonding forces with associated slip and cracking, as well as, shear deformations. The objective of the current stage is to develop a fiber model for the Timoshenko frame based on the modified cubic Hermitian polynomials and interface elements, extending the work on the classical

Bernoulli-Euler beam reported in Orakcal, Massone Sanchez, and Wallace (2006). The main purpose of using interface elements among each fiber (as is demonstrated in Fig. 1) is to improve the behavior of the proposed solution by employing shear constraint elements. To achieve this goal, the theory of fiber model based on Timoshenko straight plane frame elements is employed. Recall that, in the theory of fiber model, the interface element is not modeled as a discrete, but, each frame consists of a set of frame elements, and the analytical process is performed through a nonlinear analysis.

The suggested approach evolves from cubic Hermitian polynomials and local stress field theory. The main advantage of the developed expressions of shape functions over the classical shape functions is the shear deformation factors. Moreover, these expressions satisfied the completeness and continuity conditions. For this purpose, this research extended the work in Bazoune, Khulief, and Stephen (2003) to account shear effects of fibers by an inner sub-program based on local stress field theory. In what follows, the authors' methodology is explained in more details.

According to cubic Hermite interpolation, the degrees of freedom for each element are the displacements vector in orthogonal directions $(u, v)$ and rotational bending deformation of two neighbor nodes $(\theta)$ as Eq. (1):

$$\overline{d}(x) = \left\{ \begin{array}{c} u(x) \\ v(x) \end{array} \right\} = a_d(x).\overline{q} \quad \therefore \quad d(x) = \left\{ \begin{array}{c} \varepsilon(x) \\ \gamma(x) \end{array} \right\} = \left\{ \begin{array}{c} \dfrac{\partial(u - y\theta)}{\partial x} \\ \dfrac{\partial(u - y\theta)}{\partial y} + \dfrac{\partial v}{\partial x} \end{array} \right\} \tag{1}$$

where $x$ denotes the longitudinal axis, $u(x)$ is the axial displacement, and $v(x)$ is the transverse displacement, $y$ is the distance of a point from the centroid axis of the cross-section, and $\overline{q}$ is the nodal displacement vector as $\{u_1 \ v_1 \ \theta_1 \ u_2 \ v_2 \ \theta_2\}$. Hence, cubic Hermite interpolation matrix $a_d(x)$ is expressed as Eq. (2):

$$a_d(x) = \begin{bmatrix} \varphi_1(x) & 0 & 0 & \varphi_2(x) & 0 & 0 \\ 0 & \varphi_3(x) & \varphi_4(x) & 0 & \varphi_5(x) & \varphi_6(x) \end{bmatrix} \tag{2}$$

$$\varphi_1(x) = 1 - \frac{x}{L} \quad \therefore \quad \varphi_2(x) = \frac{x}{L}$$

$$\varphi_3(x) = \frac{1}{\Phi_z}\left(2\left(\frac{x}{L}\right)^3 - 3\left(\frac{x}{L}\right)^2 + \Phi_z\right) \therefore \varphi_4(x) = \frac{1}{2\Phi_z}\left(2L\left(\frac{x}{L}\right)^3 - (3 + \Phi_z)L\left(\frac{x}{L}\right)^2 + (1 + \Phi_z)(x)\right)$$

$$\varphi_5(x) = \frac{1}{\Phi_z}\left(-2\left(\frac{x}{L}\right)^3 + 3\left(\frac{x}{L}\right)^2 + (\Phi_z - 1)\left(\frac{x}{L}\right)\right)$$

$$\varphi_6(x) = \frac{1}{2\Phi_z}\left(2L\left(\frac{x}{L}\right)^3 + (\Phi_z - 3)L\left(\frac{x}{L}\right)^2 + (1 - \Phi_z)(x)\right)$$

$$\tag{3}$$

in these relations $\Phi_z$ is shear slenderness as Eq. (4):

$$\Phi_z = 1 + \frac{12EI_z}{\kappa_y GAL^2} \quad \therefore \quad EI_z = \sum_{n_f=1}^{n_{tf}(x)} E_{n_f} y_{n_f}^2 \tag{4}$$

in which, the variable $G$ is shear modulus obtained by a subroutine according to local stress field and direct displacement analysis which detailed explanation is given in the following. The variable $\kappa_y = (5 + 5\upsilon)/(6 + 5\upsilon)$ is defined as shear stress correction factor for rectangular sections with Poisson's ratio of $\upsilon = 0.15 \sim 0.18$ (Dong, Alpdogan, and Taciroglu 2010). In the following, element stiffness $\widetilde{K_{local}}$ is derived from the weak form of governed equations.
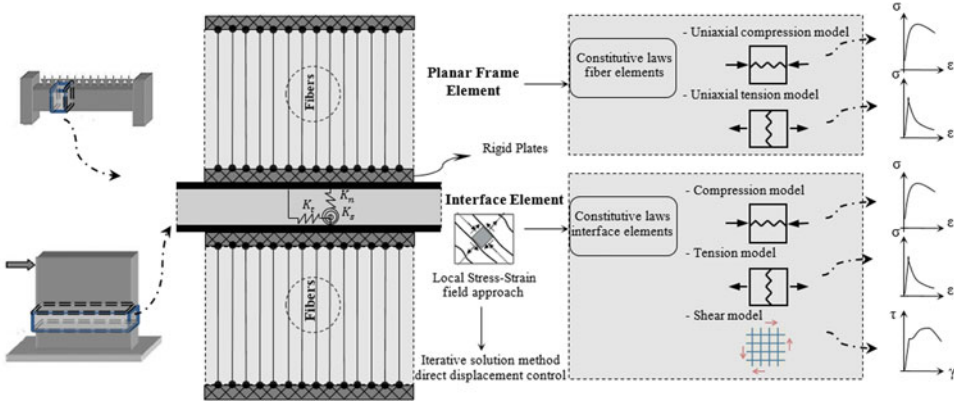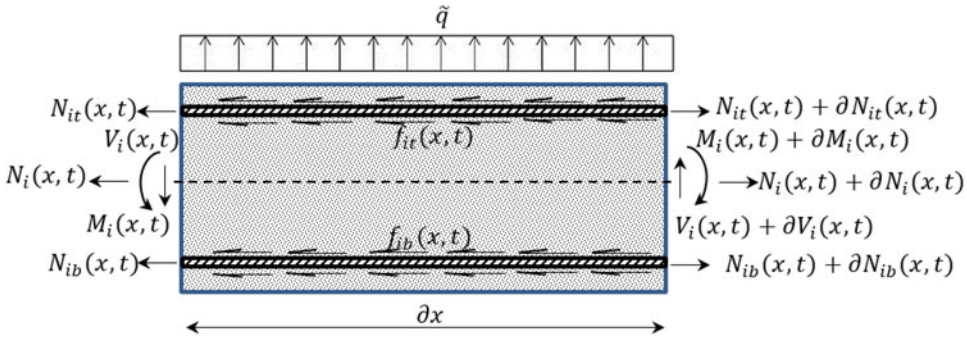
Figure 1. Proposed fiber planar frame approach.



Figure 2. Dynamic free body diagram of frame element.

$$\frac{\partial N_i(x,t)}{\partial x} = 0 \quad \therefore \quad -\frac{\partial V_i(x,t)}{\partial x} = \rho A \frac{\partial^2 V_i(x,t)}{\partial t^2} + q$$

$$-\frac{\partial^2 M_i(x,t)}{\partial x^2} = \rho A \frac{\partial^2 V_i(x,t)}{\partial t^2} + q \quad \therefore \quad -\frac{\partial N_i^{bars}(x,t)}{\partial x} + f_i^{bars}(x,t) = 0 \tag{5}$$

By using the equilibrium conditions of an infinitesimal segment $(\partial x)$ with bond interfaces at bars $\left(f_i^{bars}(x,t)\right)$ and constant external force in the $y$ direction $(\tilde{q})$, the differential (strong) form of these equations can be formulated by the dynamic free body diagram of a 2 D RC frame element as shown in Fig. 2: in these relations, each structural node has five degrees of freedom (DOF), namely, the axial equilibrium of the concrete element $(N_i(x,t))$ and steel bars $\left(N_i^{bars}(x,t)\right)$ and the vertical $V_i(x,t)$ and moment components $M_i(x,t)$ with respect to the longitudinal axis $(x)$ and time $(t)$. Also, $\rho$ and $A$ are the element material density and cross-section area, respectively. It is worth pointing out that the degrees of freedom introduced in Fig. 3 lead to a vector form $\{u\}$ as Eq. (6) consisted of axial translation of concrete $(u_N)$, vertical translation of concrete $(u_v)$, rotation about $z$-direction $(u_M)$, and axial translation of top bars $(u_{st})$ and bottom bars $(u_{sb})$, respectively. Moreover, $q$ is an external force along the element length $(L)$ and the rotation $\theta$ is positive when DOF is counter-clockwise.

$$\{u\}_i = \left\{ u_{N1} \; u_{N2} \; u_{V1} \;\; u_{M1} \;\; u_{V2} \; u_{M2} \; u_{sb1} \;\; u_{sb2} \;\; u_{st1} \;\; u_{st2} \right\}^T = \left\{ \{u_N\} \; \{u_w\} \; \{u_{slip}\} \right\}^T \tag{6}$$
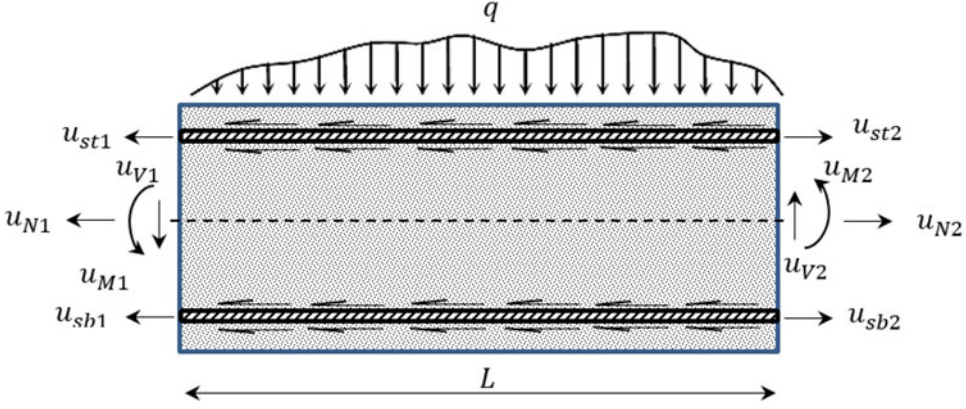
**Figure 3.** Proposed degrees of freedom.

In what follows, the internal forces of an arbitrary cross-section in the beam element are defined according to known uniaxial stress state of concrete ($\sigma_c$), concrete shear stress ($\tau_{xy}$) and stress state of bars ($\sigma s$) with the coordinate of the $i^{\text{th}}$ fiber with respect to the centroidal bending axis ($y$) as the following relations:

$$N_i(x,t) = \int_A \sigma_c \ dA + \sum_j (As_{jb}\sigma s_{jb} + As_{jt}\sigma s_{jt}) \ \therefore \ V_i(x,t) = \int_A \tau_{xy} \ dA = \kappa AG\gamma$$

$$M_i(x,t) = \int_A \sigma_c \ y \ dA + \sum_j (As_{jb}\sigma s_{jb}y_{jb} + As_{jt}\sigma s_{jt}y_{jt})$$

$$N_{ib}{}^{bars}(x,t) = \sum_j (As_{jb} \times \sigma s_{jb}) \therefore \ N_{it}{}^{bars}(x,t) = \sum_j (As_{jt} \times \sigma s_{jt})$$

$$f_{ib}(x,t) = \sum_j (\pi \times ds_{jb} \times \tau_{jb}(x,t)) \therefore \ f_{it}(x,t) = \sum_j (\pi \times ds_{jt} \times \tau_{jt}(x,t))$$

(7)

in which, the subscript $i$ is an indicator of element number, $ds$ and $As$ are circumference and area of steel bars in each fiber, $\tau$ is the local bond stress and subscript $b$ and $t$ represent bottom and top bars, respectively.

In what follows, deformation of the beam at the current configuration, as well as the displacement field vector (Eq. (8)) in the corotational system based on Timoshenko beam theory are demonstrated in Fig. 4.

$$\begin{bmatrix} u_x \\ u_y \end{bmatrix} = \begin{bmatrix} u_x{}^0 - y\sin\theta \\ u_y{}^0 + y\cos\theta - y \end{bmatrix} \ \therefore \ \theta = \frac{\partial V_i(x,t)}{\partial x} = \frac{\partial u_w}{\partial x} = \psi + \gamma \tag{8}$$

In the following, an infinitesimal element of the member axis at the current configuration is illustrated as Fig. 5.

$$\psi \approx \tan\psi = \left(\frac{du_y}{dx + du_x}\right) = \left(\frac{\left(du_y/dx\right)}{1 + \left(du_x/dx\right)}\right) = \left(\frac{u_y'}{1 + u_x'}\right) \tag{9}$$

The bending rotation of cross-section ($\psi$) is obtained by the configuration of the element and displacement at points on axis:

After deformation, an infinitesimal element length of fiber from the member axis at current configuration is given by:
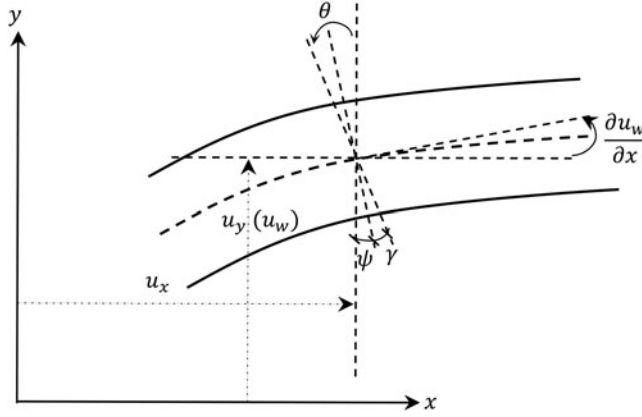
**Figure 4.** Beam configuration and displacement field considering the theory of Timoshenko beam.

$$dS' = \frac{ds}{dx} = \sqrt{(1 + u_x')^2 + u_y'^2} \tag{10}$$

Furthermore, the following relations can then be obtained:

$$\begin{aligned} 1 + u_x' &= dS' \cos \psi \\ u_y' &= dS' \sin \psi \end{aligned} \tag{11}$$

in these relations, $u_X$ and $u_Y$ $(u_w)$ are the displacements of the projection of $\Omega_0$ on the neutral axis in the $X - Y$ system. Also, $\theta$ represents the summation of bending rotation and shear rotation at the cross-section, $dS'$ as the arc length along the neutral axis in the current configuration, primes denote the derivatives with respect to $X$, and $L$ and $L_0$ are current and reference element lengths, respectively. As can be inferred in Fig. 4, the following relations can be written:

$$\sin \theta = \frac{\partial u_w}{\partial x} \rightarrow \frac{\partial^2 u_w}{\partial x^2} = \kappa \cos \theta \rightarrow \cos \theta = \frac{\partial^2 u_w}{\kappa \partial x^2} \tag{12}$$

The nonlinear strain vector ($\bar{\varepsilon}$) including the axial strain ($\varepsilon_{xx}$) and the transverse shear strain ($\varepsilon_{yx}$) defined as:

$$\bar{\varepsilon} = \left\{ \begin{array}{c} \varepsilon_{xx} \\ 2\varepsilon_{yx} \end{array} \right\} = \left\{ \begin{array}{c} e - y\kappa \\ \gamma \end{array} \right\}$$

$$\left\{ \begin{array}{c} e \\ \gamma \\ \kappa \end{array} \right\} = \left\{ \begin{array}{c} (1 + u_x') \cos \theta + u_y' \sin \theta - 1 \\ -(1 + u_x') \sin \theta + u_y' \cos \theta \\ \kappa \end{array} \right\} \tag{13}$$

in which, the three strain quantities ($e$, $\gamma$, $\kappa$) characterize axial strains, shear strains, and curvatures, respectively. The bond-slip between the surrounding concrete and the $i^{th}$ fiber of reinforcement ($u_{slip}$), the normal strain of the concrete ($\varepsilon_{xx}^{con}$), and steel bar strain of $i^{th}$ layer ($\varepsilon_{xx}^{bars}$) are defined through the following compatibility relations. It worthwhile to point out that derivative of $u_X$ and $u_Y$ with respect to $X$ can be substituted by mentioned relations in Fig. 4:

$$\begin{aligned} u_{slip} &= u_{x_i}{}^s - u_{xi} = u_{x_i}{}^s - u_x{}^0 - y \sin \theta \\ \varepsilon_{xx}{}^{con} &= (1 + u_x') \cos \theta + u_y' \sin \theta - 1 - y\kappa \\ \varepsilon_{xx}{}^{bars} &= \varepsilon_{xx}{}^{con} + \frac{\partial u_{slip}}{\partial x} \end{aligned} \tag{14}$$
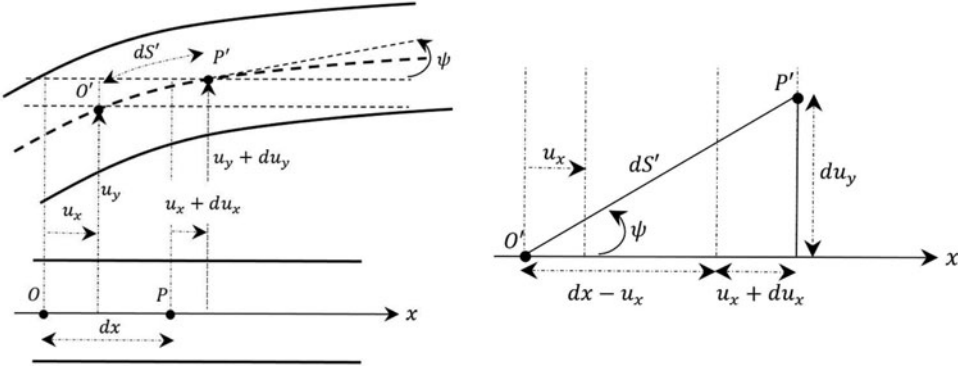
**Figure 5.** Member differential element.

where $u_{x_i}$ with the superscript $s$ is an indicator of bar slip in the $i^{\text{th}}$ fiber. By using $u'_y = (1 + u'_x)\tan\psi$ and Eq. (12), the $\varepsilon_{xx}{}^{con}$ is rewritten as:

$$
\begin{aligned}
\varepsilon_{xx}{}^{con} &= \left[ \left(1 + \frac{\partial u_N}{\partial x}\right)\cos\theta + \left(1 + \frac{\partial u_N}{\partial x}\right)\tan\psi\,\sin\theta - 1 \right] - y\kappa \\
&= \left[ \left(1 + \frac{\partial u_N}{\partial x}\right)(\sec\theta) - 1 \right] - y\kappa = \left[ \left(1 + \frac{\partial u_N}{\partial x}\right)\left(\frac{\kappa}{\frac{\partial^2 u_w}{\partial x^2}}\right) - 1 \right] - y\kappa
\end{aligned}
\tag{15}
$$

Hence, Eqs. (14) and (15) together with the equilibrium equations (Eq. (5)) make it possible to express the force-displacement relations of the strong form through stress-deformation relations.

To obtain element stiffness, the weak formulation of structural elements is extracted by using arbitrary test-functions. Thus, the variational form of Eq. (5) are turned into a weak form by left-multiplication of $\delta u_N$, $\delta u_w$, $\delta u_{slip}{}^b$ and $\delta u_{slip}{}^t$ which respectively correspond to the nodal axial displacement, nodal deflections, and rotations at the reference axis, and nodal relative slip at bottom bars and top bars as:

$$
\int_L N_i(x,t)\frac{\partial \delta u_N}{\partial x}dx = [\delta u_N\ N_i(x,t)]_0^L
\tag{16}
$$

$$
-\int_L M_i(x,t)\frac{\partial^2 \delta u_w}{\partial x^2}dx = \int_L \delta u_w\left(\rho A\frac{\partial^2 V_i(x,t)}{\partial t^2} + q\right)dx - \left[\frac{\partial \delta u_w}{\partial x}\ M_i(x,t)\right]_0^L + [\delta u_w\ V_i(x,t)]_0^L
\tag{17}
$$

$$
\int_L N_{ib}{}^{bars}(x,t)\frac{\partial \delta u_{slip}{}^b}{\partial x}dx - \int_L \delta u_{slip}{}^b f_{ib}{}^{bars}(x,t)dx = \left[\delta u_s{}^b\ N_{ib}{}^{bars}(x,t)\right]_0^L
\tag{18}
$$

$$
\int_L N_{it}{}^{bars}(x,t)\frac{\partial \delta u_{slip}{}^t}{\partial x}dx + \int_L \delta u_{slip}{}^t f_{it}{}^{bars}(x,t)dx = \left[\delta u_s{}^t\ N_{it}{}^{bars}(x,t)\right]_0^L
\tag{19}
$$

It is worth highlighting that Eqs. (16), (18) and (19) are obtained through the integration by parts once and twice for Eq. (17) over the whole domain. Also, the boundary terms can be determined by a function of the natural degrees of freedom or essential boundary conditions. In what follows, by substituting Eqs. (7), (16)–(19), the element stiffness matrix for continuum finite elements from the governing differential equation can be derived. Considering an incremental formulation of equilibrium, the tangent stiffness matrix is obtained through the first variation of the internal force vector in each degree of freedom direction. Therefore, the directional derivatives of the obtained equations in the direction of $\{\widetilde{u_N}\}$, $\{\widetilde{u_w}\}$, and $\{\widetilde{u_{slip}}\}$ can now be stated as follows. The first row of stiffness matrix is written by the directional derivative of equations in the

direction of $\{\widetilde{u_N}\}$, $\{\widetilde{u_w}\}$, and $\{\widetilde{u_{slip}}\}$ as:

$$\{\widetilde{u_N}\}_i^T \underbrace{\int_L \lambda_N \left(\frac{\kappa}{B_w\{\widetilde{u_w}\}}\right) B_N dx}_{k_{\widetilde{u_N}}^{\widetilde{u_N}}} \{\Delta\widetilde{u_N}\}_i$$

(20)

$$\lambda_N = B_N{}^T \left[ \int_A \frac{\partial\sigma_c}{\partial\varepsilon} \, dA + \sum_j \left( As_{jb} \frac{\partial\sigma s_{jb}}{\partial\varepsilon} + As_{jt} \frac{\partial\sigma s_{jt}}{\partial\varepsilon} \right) \right]$$

$$\{\widetilde{u_N}\}_i^T \underbrace{\int_L - \lambda_N \frac{\kappa(1 + B_N\{\widetilde{u_N}\})}{\{B_w\widetilde{u_w}\}^2} B_w dx}_{k_{\widetilde{u_N}}^{\widetilde{u_w}}} \{\Delta\widetilde{u_w}\}_i$$

(21)

$$\{\widetilde{u_N}\}_i^T \underbrace{\int_L \begin{bmatrix} \lambda_N^s & 0 \\ 0 & \lambda_N^s \end{bmatrix} B_{slip} dx}_{k_{\widetilde{u_N}}^{\widetilde{u_{slip}}}} \{\Delta\widetilde{u_{slip}}\}_i \quad \therefore \lambda_N^s = B_N{}^T \left[ \sum_j \left( As_{jb} \frac{\partial\sigma s_{jb}}{\partial\varepsilon} + As_{jt} \frac{\partial\sigma s_{jb}}{\partial\varepsilon} \right) \right]$$

(22)

In the following, the second row of stiffness matrix is written by the directional derivative of equations in the direction of $\{\widetilde{u_N}\}$, $\{\widetilde{u_w}\}$, and $\{\widetilde{u_{slip}}\}$ as:

$$\{\widetilde{u_w}\}_i^T \underbrace{\int_L - \lambda_w \left(\frac{\kappa}{B_w\{\widetilde{u_w}\}}\right) B_N dx}_{k_{\widetilde{u_w}}^{\widetilde{u_N}}} \{\Delta\widetilde{u_N}\}_i$$

(23)

$$\lambda_w = B_w{}^T \left[ \int_A \sigma_c y \, dA + \sum_j (As_{jb}\sigma s_{jb} y_{jb} + As_{jt}\sigma s_{jt} y_{jt}) \right]$$

$$\{\widetilde{u_w}\}_i^T \underbrace{\int_L \lambda_w \frac{\kappa(1 + B_N\{\widetilde{u_N}\})}{\{B_w\widetilde{u_w}\}^2} B_w dx}_{k_{\widetilde{u_w}}^{\widetilde{u_w}}} \{\Delta\widetilde{u_w}\}_i$$

(24)

$$\{\widetilde{u_w}\}_i^T \underbrace{\int_L - \begin{bmatrix} \lambda_w^s & 0 \\ 0 & \lambda_w^s \end{bmatrix} B_{slip} dx}_{k_{\widetilde{u_w}}^{\widetilde{u_{slip}}}} \{\Delta\widetilde{u_{slip}}\}_i \quad \therefore \lambda_w^s = B_w{}^T \left[ \sum_j (As_{jb}\sigma s_{jb} y_{jb} + As_{jt}\sigma s_{jt} y_{jt}) \right]$$

(25)

Finally, the third row of the stiffness matrix is written by the directional derivative of equations in the direction of $\{\widetilde{u_N}\}$, $\{\widetilde{u_w}\}$, and $\{\widetilde{u_{slip}}\}$ as:

$$\{\widetilde{u_{slip}}\}_i^T \underbrace{\int_L B_{slip}{}^T \lambda_{slip}^\sigma \left(\frac{\kappa}{B_w\{\widetilde{u_w}\}}\right) B_N dx}_{k_{\widetilde{u_{slip}}}^{\widetilde{u_N}}} \{\Delta\widetilde{u_N}\}_i$$

(26)

$$\lambda_{slip}^\sigma = \begin{bmatrix} \sum_j \left(As_{jb} \frac{\partial\sigma s_{jb}}{\partial x}\right) & 0 \\ 0 & \sum_j \left(As_{jt} \frac{\partial\sigma s_{jt}}{\partial x}\right) \end{bmatrix} \quad \therefore \lambda_{slip}^\tau = \begin{bmatrix} \sum_j \left(\pi \times ds_{jb} \times \frac{\partial\tau_{jb}}{\partial x}\right) & 0 \\ 0 & \sum_j \left(\pi \times ds_{jt} \times \frac{\partial\tau_{jt}}{\partial x}\right) \end{bmatrix}$$

$$\{\widetilde{u_{slip}}\}_i^T \underbrace{\int_L -B_{slip}{}^T \lambda_{slip}^\sigma \left(\frac{\kappa(1 + B_N\{\widetilde{u_N}\})}{\{B_w\widetilde{u_w}\}^2}\right) B_w dx}_{k_{\widetilde{u_{slip}}}^{\widetilde{u_w}}} \{\Delta\widetilde{u_w}\}_i$$

(27)

$$\{\widetilde{u_{slip}}\}_i^T \underbrace{\left( \int_L B_{slip}{}^T \lambda_{slip}^\sigma B_{slip} dx + \int_L N_{slip}{}^T \lambda_{slip}^\tau N_{slip} dx \right)}_{k_{\widetilde{u_{slip}}}^{\widetilde{u_{slip}}}} \{\Delta \widetilde{u_{slip}}\}_i \tag{28}$$

In conclusion, the resulting local stiffness matrix $(\widetilde{K_{local}})$ can be written by using relations (20) to (28) as the following established form:

$$\widetilde{K_{local}} = \begin{bmatrix} k_{\widetilde{u_N}}^{\widetilde{u_N}} & k_{\widetilde{u_N}}^{\widetilde{u_w}} & k_{\widetilde{u_N}}^{\widetilde{u_{slip}}} \\ k_{\widetilde{u_w}}^{\widetilde{u_N}} & k_{\widetilde{u_w}}^{\widetilde{u_w}} & k_{\widetilde{u_w}}^{\widetilde{u_{slip}}} \\ k_{\widetilde{u_{slip}}}^{\widetilde{u_N}} & k_{\widetilde{u_{slip}}}^{\widetilde{u_w}} & k_{\widetilde{u_{slip}}}^{\widetilde{u_{slip}}} \end{bmatrix} \tag{29}$$

In order to take the shear failure mode into account in formulations of this stage, it is necessary to assemble a series of elements along with fiber frame elements. These elements are known as interface elements. Several developments of interface elements were provided by researchers presented as the four-node iso-parametric elements (Goodman, Taylor, and Brekke 1968; Herrmann 1978). Usage of suitable interface elements and their assembling with fiber elements could increase the numerical strategy accuracy. Moreover, these elements should have a consistency to other elements and be capable of assemblage. In this work, a new consistent interface element is proposed with a four-node iso-parametric element in correspondence to each node with zero thickness length. Stress interface zones are described by normal and shear stress, and these are calculated based on the specific rule of such elements as Eq. (30).

$$\left\{ \begin{matrix} \tau \\ \sigma \end{matrix} \right\} = [D]\{\boldsymbol{\varepsilon}\} \therefore \{\boldsymbol{\varepsilon}\} = \left\{ \begin{matrix} \gamma_{yx} \\ \varepsilon_y \end{matrix} \right\} = \left\{ \frac{u_{upp} - u_{low}}{h} \quad \frac{v_{upp} - v_{low}}{h} \right\}^T \tag{30}$$

where $[D]$ is the elastic constitutive matrix, $\sigma$ and $\tau$ represent the normal and tangential (shear) stress, $\varepsilon_y$ and $\gamma_{yx}$ represent the normal and tangential (shear) strains, $h$ is element thickness, and, $(u_{upp}, v_{upp})$ and $(u_{low}, v_{low})$ are displacements in the upper and lower faces about Cartesian axes $(x, y)$, respectively.

In the proposed method, the springs are separated in a classification of axial $(k_n)$, rotating $(k_s)$ and shear stiffness $(k_t)$ which represents the interface behaviors. The stiffness matrix of the interface element is introduced according to the following shape:

$$K_{interface} = \begin{bmatrix} k_t & 0 & 0 & -k_t & 0 & 0 \\ 0 & k_n & 0 & 0 & -k_n & 0 \\ 0 & 0 & k_s & 0 & 0 & -k_s \\ -k_t & 0 & 0 & k_t & 0 & 0 \\ 0 & -k_n & 0 & 0 & k_n & 0 \\ 0 & 0 & -k_s & 0 & 0 & k_s \end{bmatrix} \tag{31}$$

in this matrix, $k_t$, $k_n$, and $k_s$ are stiffness of springs in shear, axial, and moment respectively. The shear stiffness $(k_s)$ is earned through relative tangential displacements between the two nodes $(x, y)$ from a displacement vector in the local coordinate and local stress field direct analysis approach. Herein, the analytical procedure of interfaces along with the related governing methodology is expressed.

In order to introduce the local stress field into the average stress of an interface element on each fiber element, a "Simultaneous-Processing" concept has been added to the main finite element body of the program to evaluate the local mechanisms by mesoscale calculations. This localized concurrent processing enriches the adopted common smeared crack by considering local and average characteristics, simultaneously (for more details, see Soltani, An, and Maekawa 2005). It concentrates on the probable local mechanisms between cracks length, therefore it can easily evaluate the effect of any parameter, e.g., rebar diameter, reinforcement
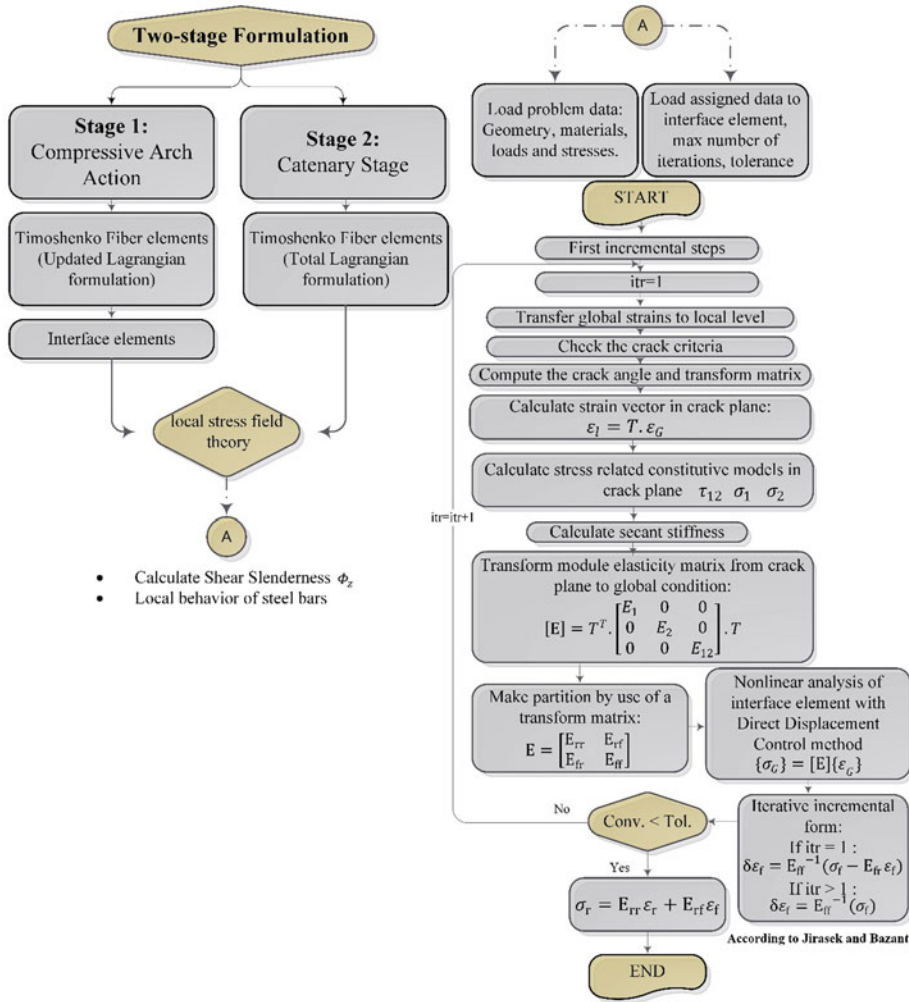
**Figure 6.** Flowchart of two-stage nonlinear analysis.

ratio, and direction, and crack direction on the cracking procedure and the average behaviors of steel bars and concrete.

The proposed simultaneous-processing also obtain more exact values for displacement domain (i.e., crack spacing, opening and sliding among classic smeared crack approaches). Accordingly, the direct displacement-based constitutive models are implemented with no simplifications nor conservative assumptions through the main finite element body of the program in each computational step state. The nonlinear behavior of the RC element can be obtained using an iterative solution method by applying in-plane incremental stresses or strains. The analytical process is executed by a implementation of direct displacement control with performing the iterative procedure that was introduced by Jirásek and Bazant (2002). In the numerical process, the structural secant stiffness matrix relates the increments of load to corresponding increments of displacement.

Finally, shear stress and shear modulus ($G_{shear}$) are extracted from each shear strain with shear cross-section area of each fiber ($A_s$) and fiber element length ($L$). Hence, Eq. (32) should be satisfied by employing stiffness of computed shear spring ($K_t$). The interface stiffness matrix is obtained. It

should be mentioned that very large amounts are considered for axial springs ($K_n$) and rotating springs ($K_s$).

$$K_t = G_{shear} \frac{A_s}{L} \tag{32}$$

Moreover, analysis of panel based on the local stress field approach is implemented using secant stiffness ($G_{shear}$). For detail, the algorithm of interface element analysis is organized in the following subsequent flowchart as Fig. 6.

## 3. Stage 2: Kinematics of total lagrangian in catenary stage

The aim of this stage is to present a developed fiber element even when displacements are large. This new scheme can be applied for studying the catenary stage beside Stage 1. For this purpose, the current stage should construct separately in considering inelastic large displacements in companion with material nonlinear constitutive laws.

In this section, the general formulations of total Lagrangian (TL) kinematics are implemented to derive the finite element equations of a two-node plane beam element. Formulations are used based on Timoshenko model with local first-order effects of shear deformation. Also, the theory can account for geometrically nonlinear behavior due to large displacements and rotations besides material nonlinearity due to constitutive behavior of each set of fiber elements (for more details, see Felippa 2001; Yousefi, Esfahani, and Tavakkolizadeh 2018). In the following, the paper summarizes the most important steps of its implementation.

Under the planar frame assumptions, the following basically relations can be obtained as Eq. (33):

$$\begin{bmatrix} x \\ y \end{bmatrix} = \begin{bmatrix} X + u_x - Y\sin\theta \\ u_y + Y\cos\theta \end{bmatrix} \quad \therefore \ \theta = \gamma + \psi \tag{33}$$

in which, $u_X$ and $u_Y$ are the displacements of the projection of $\Omega_0$ on the neutral axis in the $X - Y$ system. In addition, $\theta$ represents the rotation of the cross-section and primes denote the derivatives with respect to $X$.

The deformation gradient matrix ($F$) and displacement gradient matrix ($G$) are derived from Eq. (33) as follows:

$$F = \begin{bmatrix} \dfrac{\partial x}{\partial X} & \dfrac{\partial x}{\partial Y} \\ \dfrac{\partial y}{\partial X} & \dfrac{\partial y}{\partial Y} \end{bmatrix} = \begin{bmatrix} 1 + u'_x - Y\kappa\cos\theta & -\sin\theta \\ u'_y - Y\kappa\sin\theta & \cos\theta \end{bmatrix} \quad \therefore \ G = F - I \tag{34}$$

Strain-displacement relations can be written according to Eq. (34). The plane portion of the Green-Lagrange (GL) strain tensor ($_0^2\varepsilon_{ij}{}^0$) is obtained by Eq. (35):

$$_0^2\varepsilon_{ij}{}^0 = \varepsilon = \frac{1}{2}\left(\frac{\partial^2 x_k}{\partial^0 x_i}\frac{\partial^2 x_k}{\partial^0 x_j} - \delta_{ij}\right) = \begin{bmatrix} \varepsilon_{xx} & \varepsilon_{xy} \\ \varepsilon_{yx} & \varepsilon_{yy} \end{bmatrix} \Rightarrow 2\varepsilon = (F^T F - I) = G + G^T + G^T G \tag{35}$$

In the following, a consistent-linearization technique is used by definition an orthogonal matrix ($\Lambda$):

$$\Lambda = \begin{bmatrix} \cos\theta & \sin\theta \\ -\sin\theta & \cos\theta \end{bmatrix} \quad \therefore \ \overline{F} = \Lambda\ F = \begin{bmatrix} (1 + u'_x)\cos\theta + u'_y\sin\theta - Y\kappa & 0 \\ -(1 + u'_x)\sin\theta + u'_y\cos\theta & 1 \end{bmatrix} = \Gamma + I \tag{36}$$

Therefore, the Green strain matrix can be rewritten and replaced by the simpler form as Eq. (37):

$$2\boldsymbol{\varepsilon} = \left(\overline{\boldsymbol{F}}^T\overline{\boldsymbol{F}} - I\right) = \left((\boldsymbol{\Gamma} + I)^T(\boldsymbol{\Gamma} + I) - I\right) = \boldsymbol{\Gamma}^T + \boldsymbol{\Gamma} + \boldsymbol{\Gamma}^T\boldsymbol{\Gamma} \overset{\boldsymbol{\Gamma}^T\boldsymbol{\Gamma}\approx 0}{\Longrightarrow} \boldsymbol{\varepsilon} = \boldsymbol{\Gamma} = \begin{bmatrix} \varepsilon_{xx} & \varepsilon_{xy} \\ \varepsilon_{yx} & \varepsilon_{yy} \end{bmatrix} \quad (37)$$

Hence, the axial strains ($\varepsilon_{xx}$) and shear strains ($\varepsilon_{yx}$) can be arranged in a strain vector ($\overline{\varepsilon}$) (as Eq. (38)):

$$\overline{\varepsilon} = \left\{ \begin{array}{c} \varepsilon_{xx} \\ 2\varepsilon_{yx} \end{array} \right\} = \left\{ \begin{array}{c} e - Y\theta' \\ \gamma \end{array} \right\} \therefore \mathcal{H} = \left\{ \begin{array}{c} e \\ \gamma \\ \kappa \end{array} \right\} = \left\{ \begin{array}{c} \dfrac{L}{L_0}\cos\psi\cos\theta + \dfrac{L}{L_0}\sin\psi\sin\theta - 1 \\ -\dfrac{L}{L_0}\cos\psi\sin\theta + \dfrac{L}{L_0}\sin\psi\cos\theta \\ \theta' \end{array} \right\}$$

$$= \left\{ \begin{array}{c} s'\cos(\psi - \theta) - 1 \\ -s'\sin(\theta - \psi) \\ \theta' \end{array} \right\} \quad (38)$$

where the three strain quantities ($e$, $\gamma$, $\kappa$) characterize axial strains, shear strains and curvatures, respectively. In the following, strain displacement relation can be obtained by nodal displacement variations ($\overline{\boldsymbol{B}}$) as Eq. (39).

$$\delta\mathcal{H} = \begin{bmatrix} \delta e & \delta\gamma & \delta\kappa \end{bmatrix}^T = \overline{\boldsymbol{B}}\begin{bmatrix} \delta u_{X1} & \delta u_{Y1} & \delta\theta_1 & \delta u_{X2} & u_{Y2} & \delta\theta_2 \end{bmatrix}^T$$

$$\overline{\boldsymbol{B}} = \frac{1}{L_0} \begin{bmatrix} -\cos\omega & -\sin\omega & \gamma\varphi_{4,x}(x)L_0 & \cos\omega & \sin\omega & \gamma\varphi_{6,x}(x)L_0 \\ \sin\omega & -\cos\omega & -(1+e)\varphi_{4,x}(x)L_0 & -\sin\omega & \cos\omega & -(1+e)\varphi_{6,x}(x)L_0 \\ 0 & 0 & -1 & 0 & 0 & 1 \end{bmatrix}$$

$$(39)$$

The discretization of the variables is performed using the shape functions of the reference element. To approximate the deformations of element nodes, cubic Hermitian polynomials are formulated. Based on these interpolations the degrees of freedom for each element are the displacements in orthogonal directions and slopes at the two nodes.

$$\theta(x) = \begin{bmatrix} \varphi_{3,x}(x) & \varphi_{4,x}(x) & \varphi_{5,x}(x) & \varphi_{6,x}(x) \end{bmatrix} * \begin{bmatrix} v_1 & \theta_1 & v_2 & \theta_2 \end{bmatrix}^T \quad (40)$$

in which, $\varphi_{3,x}(x)$, $\varphi_{4,x}(x)$, $\varphi_{5,x}(x)$ and $\varphi_{6,x}(x)$ are defined as mentioned in section 2. Moreover, $\Phi_z$ is presented as the shear slenderness. The section resistance forces ($\mathcal{F}_s$) are computed from the fiber stress distribution and section stiffness ($K_s(x_i)$) is assembled from the fiber stiffness based on the given stress of the fiber state. This force vector is implemented according to Eq. (41), and the following stages lead to the calculation of element resistance force:

$$K_s(x_i) = \begin{bmatrix} \displaystyle\sum_{n_f=1}^{n_{tf}(x)} E_{n_f}A_{n_f} & 0 & -\displaystyle\sum_{n_f=1}^{n_{tf}(x)} E_{n_f}A_{n_f}y_{n_f} \\ 0 & \displaystyle\sum_{n_f=1}^{n_{tf}(x)} G_{n_f}A_{n_f} & \displaystyle\sum_{n_f=1}^{n_{tf}(x)} G_{n_f}A_{n_f}y_{n_f} \\ -\displaystyle\sum_{n_f=1}^{n_{tf}(x)} E_{n_f}A_{n_f}y_{n_f} & \displaystyle\sum_{n_f=1}^{n_{tf}(x)} G_{n_f}A_{n_f}y_{n_f} & \displaystyle\sum_{n_f=1}^{n_{tf}(x)} E_{n_f}A_{n_f}y_{n_f}^2 \end{bmatrix} \therefore \mathcal{F}_s = \left\{ \begin{array}{c} N \\ V \\ M \end{array} \right\} = \left\{ \begin{array}{c} \int \overline{\sigma}\, ds \\ \int G\gamma\, ds \\ \int \overline{\sigma}y\, ds \end{array} \right\}$$

$$= \left\{ \begin{array}{c} \displaystyle\sum_{n_f=1}^{n_{tf}(x)} E_{n_f} A_{n_f} e \\ \displaystyle\sum_{n_f=1}^{n_{tf}(x)} G_{n_f} A_{n_f} \gamma \\ \displaystyle\sum_{n_f=1}^{n_{tf}(x)} E_{n_f} {y_{n_f}}^2 \kappa \end{array} \right\} \tag{41}$$

By using principle of increment of virtual displacements, the following incremental virtual work is obtained based on the last known calculated configuration for a planar beam-column element:

$$\int E \varepsilon_{ij} \delta \varepsilon_{ij} \,^1 dV + \int \tau_{ij} \delta \eta_{ij} \,^1 dV + {}^1_1 R^1 = {}^2_1 R^1 \tag{42}$$

$$U = \frac{1}{2} \int \varepsilon_{ij}^T K_s(x_i) \varepsilon_{ij} \, dV = \frac{1}{2} \left( \int_{L_0} \left( \sum_{n_f=1}^{n_{tf}(x)} \left( E_{n_f} A_{n_f} e^2 \right) + \left( \sum_{n_f=1}^{n_{tf}(x)} G_{n_f} A_{n_f} \gamma^2 \right) + \left( \sum_{n_f=1}^{n_{tf}(x)} E_{n_f} {y_{n_f}}^2 \kappa^2 \right) \right) \right) dX \tag{43}$$

$$\begin{aligned} \delta U &= \int_{L_0} \left( \sum_{n_f=1}^{n_{tf}(x)} \left( E_{n_f} A_{n_f} e \right) \delta e + \left( \sum_{n_f=1}^{n_{tf}(x)} G_{n_f} A_{n_f} \gamma \right) \delta \gamma + \left( \sum_{n_f=1}^{n_{tf}(x)} E_{n_f} {y_{n_f}}^2 \kappa \right) \delta \kappa \right) dX \\ &= \int_{L_0} \left( \delta h^T . \mathcal{F}_s \right) dX = \int_{L_0} \left( \bar{B} . \delta u \right)^T \mathcal{F}_s \, dX \\ &= \delta u \int_{L_0} \bar{B}^T \mathcal{F}_s \, dX = \delta u \sum_{i=1}^{n_{GP}} w_i . \bar{B}(x_i)^T . \mathcal{F}_s(x_i) \end{aligned} \tag{44}$$

$$\delta U = F_{int} \delta u \quad \rightarrow \quad F_{int} = \int_{L_0} \bar{B}^T \mathcal{F}_s \, dX = \sum_{i=1}^{n_{GP}} w_i . \bar{B}(x_i)^T . \mathcal{F}_s(x_i)$$

Based upon a total Lagrangian approach, the incremental matrix equilibrium equation for a system can be formulated using the variation of the increment of total potential energy and governed equations are simplified as:

$$\begin{aligned} \delta F_{int} &= \delta \left( \int_{L_0} \bar{B}^T \mathcal{F}_s \, dX \right) = \int_{L_0} \left( \bar{B}^T \delta \mathcal{F}_s + \delta \bar{B}^T \mathcal{F}_s \right) \, dX \\ &= \int_{L_0} \left( \bar{B}^T K_s \bar{B} . \delta u + \frac{\partial \bar{B}^T}{\partial u} \delta u \, \mathcal{F}_s \right) \, dX = \left( K_{Mat.} + K_{Geo.} \right) \delta u \end{aligned} \tag{45}$$

$$\delta \mathcal{F}_s = K_s \delta h = K_s \bar{B} . \delta u$$

in which, $K_{Mat.}$ and $K_{Geo.}$ are the stiffeness of fiber planar Timoshenko frame element due to material and geometric nonlinearity, respectively.

$$K_{Mat.} = \int_{L_0} \left( \bar{B}^T K_s \bar{B} \right) \, dX = \frac{L_0}{2} \sum_{i=1}^{n_{GP}} w_i . \left( \bar{B}(x)^T . K_s(x) . \bar{B}(x) \right)_{x = \frac{L_0}{2}(1+x_i)} \tag{46}$$

$$K_{Geo.} = \int_{L_0} \left( \frac{\partial \overline{B}^T}{\partial u} \; \mathcal{F}_s \right) \, dX = \int_{L_0} \left( \frac{\partial \overline{B}^T}{\partial u} \; \left\{ \begin{array}{c} N \\ V \\ M \end{array} \right\} \right) \, dX \qquad (47)$$

in these relations, $\frac{\partial \overline{B}^T}{\partial u}$ is the first variation of $\overline{B}$ respect to increment of displacement.

## 4. Two-stage solution procedure

In the previous sections, the kinematics of the planar fiber element were presented. To simulate the removal of a load-bearing element scenario, interface elements among each fiber elements are assembled. In addition, the shear behavior and bond-slip effect were considered based on local stress field theory. Here, an incremental solution approach has been proposed, based on a mixed formulation in terms of displacements, strains, stresses, damages and load parameters in the incremental step. To switch from a small-displacements analysis to a large-displacements analysis, a criterion should be defined. For this purpose, it can be assumed that large displacements occur beyond an elastic limit. The limit elastic displacement is related directly to the rotation at bars yielding. This criterion is usually achieved at vertical displacement of beam depth which compressive arc action is ended. The mentioned stages are gathered together to trace the behavior of RC structures in the field of small displacements and large displacements, simultaneously.

To overcome disadvantages of each approach, a new two-stage formulation is proposed to ameliorate RC element simulations without losing accuracy and instability problems which can be developed for general cases (i.e., arbitrary materials, geometrics, loadings, and incremental steps). Moreover, a new formulation to attain the shear response along with flexural behavior for any load cases is suggested as local stress field model in interface elements.

## 5. Constitutive models

### 5.1. Compression behavior

Under uniaxial compression or biaxial compressive stress state of the material, nonlinear material characteristics are considered. A realistic stress-strain model is used for concrete behavior in compression, a linear response is considered for the uncracked region in a concrete constitutive model and an exponential relationship is employed in the crack region which requires three parameters (for more details, see Maekawa, Okamura, and Pimanmas (2003), and Ghorbi, Soltani, and Maekawa (2013)). The constitutive relation in the uncracked state is restricted to linear elasticity. When tension criterion is violated, this linear elastic relation is replaced by exponential forms.

In this research, a function of strains in the perpendicular direction is used referring to Collins, Vecchio, and Mehlhorn (1985), for uniaxial compression model. The decrease in the stiffness of the cracked RC element is implemented by multiplying the compressive stress by strength reduction factor ($\beta$) as Fig. 7 in these relations, $\varepsilon_1$ is the tensile strain in the principal direction 1.

### 5.2. Tension behavior

The concrete constitutive model in tension is usually regarded as linear until the tension strength ($f_t$) has been reached. After cracking strain ($\varepsilon_{cr}$), crack localization of a narrow process zone and crack initiation occurs. Subsequently, the tension-softening model is usually expressed as a relationship between crack width and bridging stress (Okamura and Maekawa 1991). Here the model
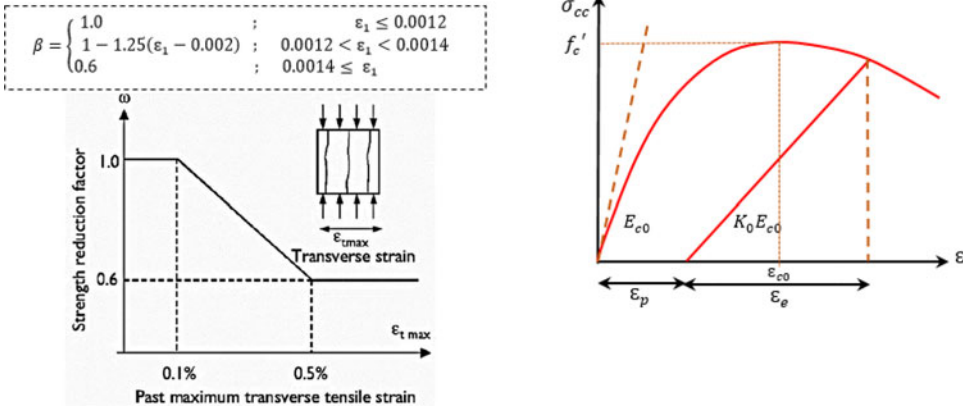
**Figure 7.** Strength reduction factor.

of Vecchio and Collins (1986) is adopted for analysis which is an exponential post-cracking softening model for concrete units.

### 5.3. Shear behavior

The constitutive shear model is adapted according to Li (1989) which was developed for modeling the nonlinear behavior of concrete elements. This shear model is embedded based on local stress-field approach applied in sub-program. More details are explained in Section 2.

### 5.4. Local behavior of steel bars

An accurate local bond-slip model is of fundamental importance in the modeling of RC structures, particularly for membrane behavior cases. In other words, the bond stress transfer between steel bar and concrete on the distribution of local strain of rebar is noticeable. For this purpose, steel-concrete interaction mechanisms are considered with an inner iterative computational approach (Soltani, An, and Maekawa 2003).

In the present paper, the universal bond-slip-strain model proposed by Shima, Chou, and Okamura (1987) which is applicable for both elastic and post-yield ranges, is used. The effect of elasticity, hardening strain and the stiffness in strain hardening zone, in other words, the strain-stress characteristics of bare bar, is considered in this model.

In addition to the common features of the bond stress distribution, the specific bond deterioration in near crack locations is also estimated in the iterative approach. In order to consider this effect, the 'Bond Deterioration Zone' is considered beside the crack surface, as introduced by Qureshi (1933), which is a function of bar diameter.

### 6. Nonlinear solution algorithm

In this section, two numerical methods for solving the nonlinear equations is implemented. At first, the arc-length method is adopted to solve the incremental equilibrium which deployed for self-adaptive changing of the loading direction at the limit points beside numerical stability at the critical points. Schweizerhof and Wriggers (1986) are proposed a direct solution by means of the two iterative displacement vectors known as a linearized arc-length method. Afterward, a direct displacement control method is implemented in sub-program to evaluate local stress bars in RC structures. In this work, the most important steps of each method are described below.

For a problem with $n$ displacement variables in the load level $(\lambda)$, the following relations are considered by Schweizerhof and Wriggers (1986):

$$\begin{pmatrix} \delta d^i \\ \delta \lambda^i \end{pmatrix} = - \begin{bmatrix} K_t & -q_e \\ 2(\varDelta d^i)^T & 2\varDelta\lambda^i \delta\lambda^i \psi^2 q_e^{\,T} q_e \end{bmatrix}^{-1} \begin{pmatrix} r^i \\ a^i \end{pmatrix} \tag{48}$$

where $K_t$ is the tangent stiffness matrix, $r^i$ is constraint equation, $q_e$ is the nodal load pattern, $a^i = (\varDelta d^i)^T \varDelta d^i + (\varDelta\lambda^i)^2 \psi^2 q_e^{\,T} q_e - \varDelta l^2$, in which, $\varDelta l$ is the fixed radius of the desired intersection with the equilibrium path, also known as incremental length, $\psi$ is the scaling parameter to combine different dimensions for the load and displacement terms. This value is chosen zero for displacement control criteria, and the vector $\varDelta d^i$ and the scalar $\varDelta\lambda^i$ are increments and are related back to the last converged equilibrium state. This approach is known as Linearized arc-length method. A convenient decomposition is described as follow:

$$\delta d^i = -K_t^{-1} r^i + \delta\lambda^i \delta d_t^{\,i} \tag{49}$$

$$\delta d^i = \delta\overline{d}^i + \delta\lambda^i \delta d_t^{\,i} \tag{50}$$

$$\delta\overline{d}^i = -K_t^{-1} r^i \therefore \delta d_t^{\,i} = K_t^{-1} q_e \tag{51}$$

Therefore the iterative load level $\delta\lambda^i$ is yielded by using the Taylor expansion:

$$\delta\lambda^i = \frac{-\left(\frac{a^i}{2}\right) - (\varDelta d^i)^T (\delta\overline{d}^i)}{(\varDelta d^i)^T (\delta d_t) + \varDelta\lambda^i \psi^2 q_e^{\,T} q_e} \tag{52}$$

Hence, the new incremental displacements and load level are determined:

$$\begin{aligned} \varDelta d^{i+1} = \varDelta d^i + \delta d^i \\ \varDelta\lambda^{i+1} = \varDelta\lambda^i + \delta\lambda^i \end{aligned} \tag{53}$$

To predict the continuation direction of the equilibrium path, the criterion proposed by Feng, Perić, and Owen (1995) is considered as Eq. (54) which is insensitive to limit points, turning points and bifurcation points.

$$sign(\varDelta\lambda^1) = sign\left(\{\varDelta d^0\}^T \delta d_t^{\,0}\right) \tag{54}$$

In the following, the second algorithm is implemented in a RC interface element analysis based on the well-known Newton–Raphson method. The nonlinear behavior of the membrane element can be obtained using an iterative solution method by applying in-plane incremental stresses or strains. The analytical process is executed by the implementation of direct displacement control that was introduced by Jirásek and Bazant (2002) as Eq. (55) which displacement vector is divided into two groups. The first one contains unknown displacements at nodes that are left free ($\varDelta U_{f,n}^i$), and the second one consists of prescribed displacements at nodes that are controlled ($\varDelta U_{r,n}^i$). Please refer to Jirásek and Bazant (2002) for more details on the algorithm and variables.

$$\begin{aligned} \begin{pmatrix} R_{f,n} - P_{f,n}^i \\ R_{r,n} - P_{r,n}^i \end{pmatrix} &= \begin{bmatrix} K_{ff,n}^i & K_{fr,n}^i \\ K_{rf,n}^i & K_{rr,n}^i \end{bmatrix} \begin{pmatrix} \varDelta U_{f,n}^i \\ \varDelta U_{r,n}^i \end{pmatrix} \\ \varDelta U_{f,n}^i &= K_{ff,n}^{i\,-1} \left( R_{f,n} - P_{f,n}^i - K_{fr,n}^i \varDelta U_{r,n}^i \right) \\ R_{r,n} &= K_{rr,n}^i \varDelta U_{r,n}^i + K_{rf,n}^i \varDelta U_{f,n}^i + P_{r,n}^i \end{aligned} \tag{55}$$

in these relations, $R_{f,n}$ and $R_{r,n}$ are external force vectors at nodes that are left free and controlled, respectively. Also, $P_{f,n}^i$ and $P_{r,n}^i$ are internal force vectors at nodes that are left free and

controlled in each increment step, respectively. The matrix $K^i_{ff,n}$, $K^i_{fr,n}$, $K^i_{rf,n}$, and $K^i_{rr,n}$ are partitioned form of tangent stiffness ($K_t$) for free nodes and controlled nodes in increment step of $i$. Based on the aforementioned aspects, the approach is implemented in a specific program organized on two level bases. A Newton-Raphson iteration loop at the interface level and another iteration loop at each element state determination of element level in fiber planar frame element.

## 7. Numerical implementation and solution

In the previous sections, the theoretical models for simulation of a fiber element with the frame approach were summarized. Here, an incremental solution approach has been followed based on the governed formulations in terms of displacements, strains, stresses, damages, and, load parameters in the incremental step. Previously mentioned formulations are gathered together to trace the behavior of RC structures in the field of membrane action behavior. The following four sets of numerical examples are used to illustrate the validity and efficiency of the proposed fiber element.

### 7.1. Validation of interface elements

In this section, in order to introduce the local stress field into the average stress-strain of interface elements, a separate program is implemented to evaluate probable local mechanisms between cracks length. To verify the accuracy of the sub-program performed at the element level, a set of panels tested by Vecchio and Collins (1986) and Pang and Hsu (1995) were analyzed under uniform stresses inside the plate as Fig. 8:

In specimen PV3 and PV4, shear slip is not activated at the crack interface due to isotropically arrangement of reinforcements in two directions. Moreover, the compressive stress parallel to the crack direction is not large enough to show great influence. Thus these specimens can be used to check the tension stiffening and reinforcing bar model. As can be inferred in theory, the
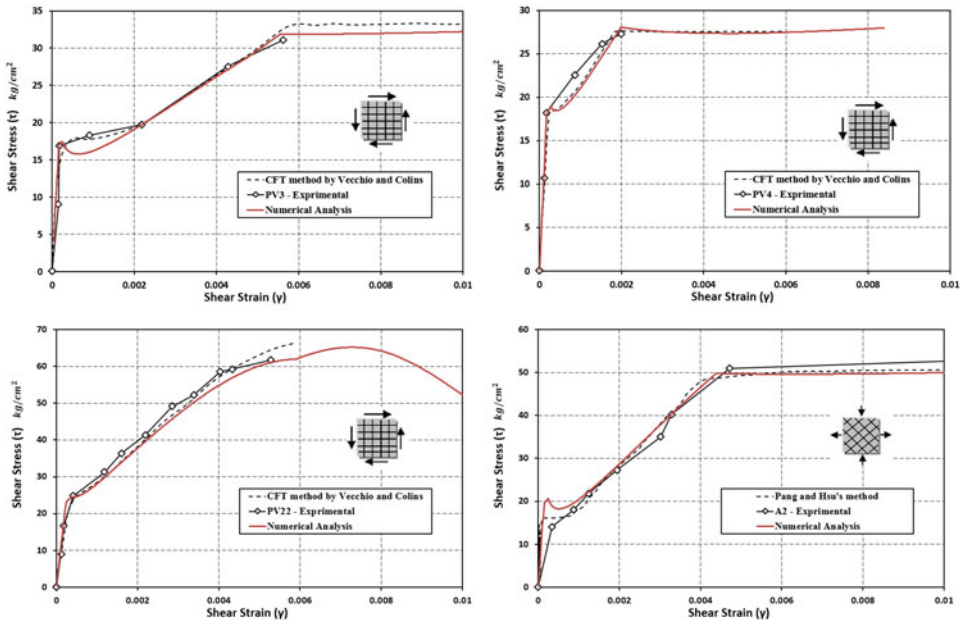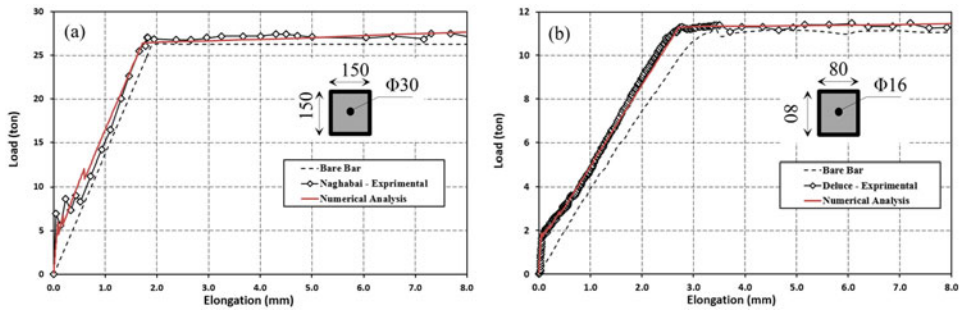


Figure 8. The panel analysis results.

**Figure 9.** Comparison between analytical approach predictions and (a) Noghabai's experiments and (b) Deluce's experiments.

average yield strength of bar embedded in concrete is smaller that of a single bare-bar due to bonding effects (Soltani, An, and Maekawa 2003). In addition, the average yield stress of bar in PV4 and A2 is assumed to be equal to bare bar yield strength. In the PV4 and A2 panel, results show greatly overestimate of yield strength and initial stiffness in comparison with the experimental one, respectively. Also, the ultimate capacity of PV22 is governed by concrete compression failure and the influence of the degradation effect due to orthogonal tensile strain is demonstrated.

Based on the mentioned scheme, the local bond-slip-strain relation is calibrated on the base of the results of experimental investigations previously performed by the authors. Noghabai (2000) and Deluce (2011) results from experiments aimed at better understanding the influence of tension stiffening on reinforcing bars embedded in concrete prisms. To ensure the reliability of local strain profile for embedded steel bars in related fibers, the comparative analysis was done between the experimental and predicted load-strain and tension stiffening relations as Fig. 9.

Hence, comparison with an experimental tests shows that the existed local constitutive steel model based on iterative approach and adapted local bond-slip-strain relationship could yield accurate and convergent results in agreement with the problems. Thus, implemented existed local steel behavior model can be used in the main program.

## 7.2. Validation of stage 1: updated lagrangian

In what follows, the iterative-incremental method with a variable stiffness scheme was applied to analyze RC structures. Thus, the ability of the proposed method to predict the nonlinear behavior of the different cases is validated in this section by comparing the analytical and experimental results of the tests performed by Palermo and Vecchio (2003), and Chun and Kim (2004).

As the first specimens, three shear wall cases were studied and the proposed analytical results were compared with the corresponding experimental results. The Palermo and Vecchio's experimental test as shown in Fig. 10 is consisted of a shear panel and two lateral flanges, at the top and bottom of them have placed two concrete slabs. The RC wall geometry consists of $1910 \times 102 \times 4570 \ mm^3$ and two flanges of $305 \times 305 \times 4570 \ mm^3$ with the additional boundary condition given by two concrete slabs placed at the top and bottom of the specimen (for more details, see Palermo and Vecchio (2003)). The equilibrium path was constructed by 180 unequal steps and an absolute norm of displacement with a 0.001 convergence tolerance was adopted. Accordingly, the results of the nonlinear computer analysis are compared with the available experimental data as Fig. 10.

It is observed that the value of the yield point load predicted by the presented approach $P = 58$ ton (at horizontal displacement of 20 mm) correlates relatively well with the experimental result of $P = 60$ ton (at horizontal displacement of 24 mm). Moreover, the post-pick behavior of
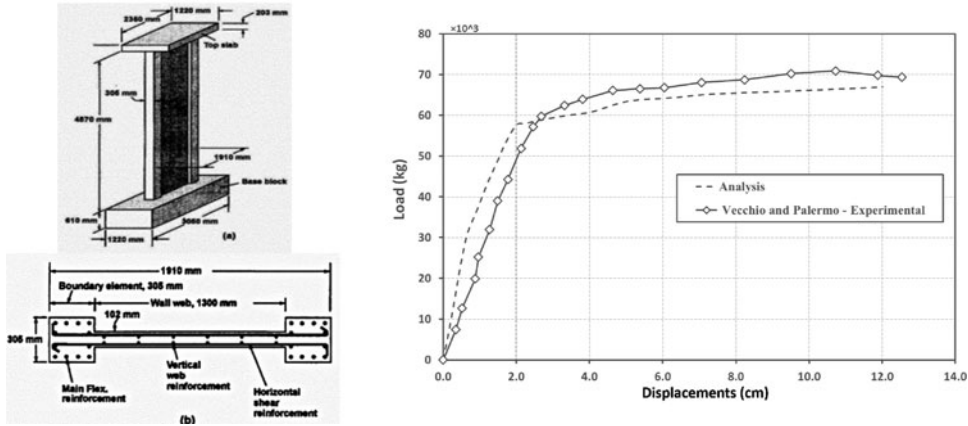
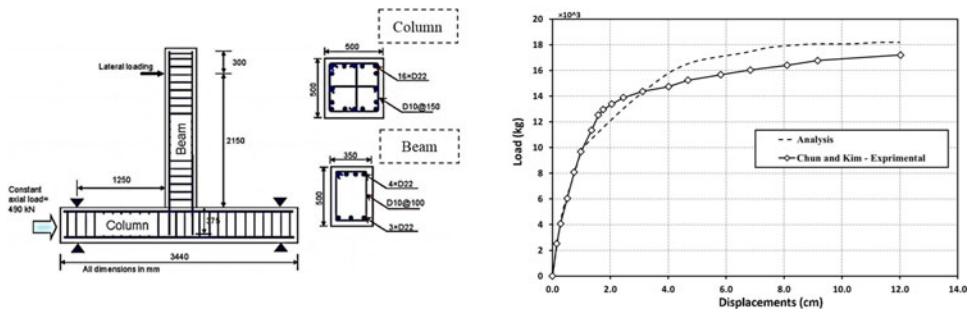**Figure 10.** Performed test by Palermo and Vecchio (2003).



**Figure 11.** Performed test by Chun and Kim (2004).

response is reasonably estimated. Also, the difference of first secant stiffness is implicit in fiber formulations and test setup assumption.

In the following, to evaluate the performance of updated Lagrangian formulation, an exterior beam-column joint tested by Chun and Kim was simulated (For more details, see Chun and Kim (2004)). From the beam flexural failing experiments, the specimen had similar yield strength, yield displacement, and member capacity through a comparison with proposed approach as Fig. 11.

As a result, the contribution of flexural deformations and shear effects can cover experimental result in a reasonable manner as well. Moreover, the adaptability and capability of interface-fiber elements based on local stress field approach had more accuracy in governed flexural modes at the initial stages (e.g., medium span-to-depth ratios and joint connections).

## 7.3. Validation of stage 2: total lagrangian

In this section, the iterative-incremental method (linearized arc-length method) with a variable stiffness scheme was applied to analyze cased. Hence, several numerical investigations were performed with the proposed model in order to study the effects of nonlinear shear deformations and flexural responses, simultaneously. These examples are considered as "classic" benchmark since some of them have been widely used by several researchers to evaluate their nonlinear frame models. At first, a cantilever beam subjected to an end-point was illustrated in Fig. 12. This classical problem had been analyzed by many researchers, including Bathe and Bolourchi (1979), and Limkatanyu et al. (2014). It consists of a prismatic fiber beam with total cross-section area $A = 1.27 \times 10^{-2}\ m^2$ with 20 fiber in each 10 set of elements, the moment of inertia
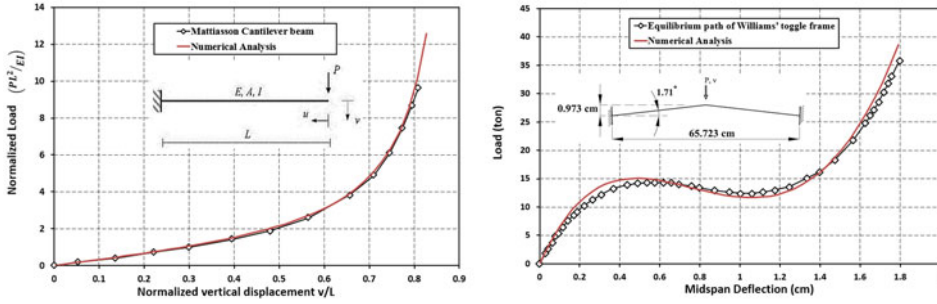
**Figure 12.** Load-vertical displacement responses for (Left) a cantilever beam and (Right) Williams' Toggle frame.
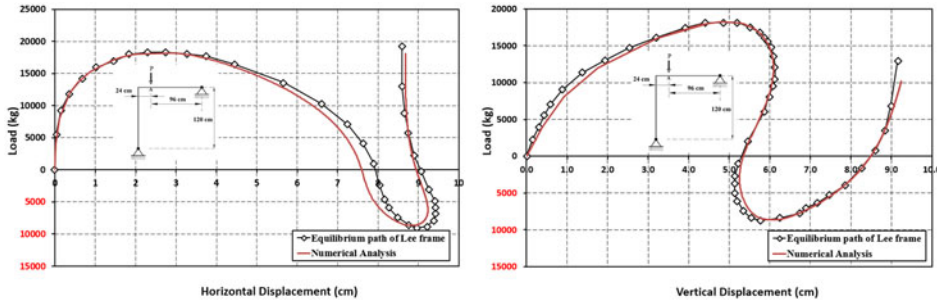


**Figure 13.** Load-displacement responses for Lee et al.'s frame (Left) load-vertical displacement diagram and (Right) load-horizontal displacement diagram.

$I = 3.66 \times 10^{-6} \ m^4$, length $L = 4 \, m$, and elastic modulus $E = 200 \, GPa$. The obtained results are compared with the elliptic integral solutions as Fig. 12 (Left).

In the following, Williams' Toggle frame's example is solved analytically (Williams 1964). It was a toggle frame with two fixed ends, with rectangular shape cross-section of $19.13 \, mm \times 6.17 \, mm$, modulus of elasticity was $71018 \, MPa$, the number of fiber cells and the number of element was 20. The number of iterations required for convergence criteria varied from 5 to 10 at different displacement step levels. The results indicate good agreement between the present solutions and existed solutions as shown in Fig. 12 (Right).

The analytical solution to the frame problem shown in Fig. 13 was given by Lee et al.'s frame (Limkatanyu et al. 2014). This model is employed to assess the capability of present formulation in a snap-back instability phenomenon. In the analysis process, every element was devised into ten elements, the cross-section was devised into 20 fibers. Good agreement between the analytical and the numerical responses is clearly observed in vertical and horizontal reference point under applied load.

## 7.4. Validation of two-stage numerical approach

Based on the mentioned scheme, the implemented program can cover different structures in small displacement domains (section 2) and large displacement cases (section 3). In this section, the ability of the proposed method to predict the nonlinear behavior of the structures in column collapse scenario is validated by comparing the numerical and experimental results of the tests performed by Sasani, Werner, and Kazemi (2011), and Pham, Tan, and Yu (2017) (as Fig. 15 and Fig. 17). Rebar detailing and material test of all specimens are presented in Sasani, Werner, and Kazemi (2011) and Pham, Tan, and Yu (2017), while Fig. 14 and Fig. 16 shows the configuration of the tests. As specific details on section width and concrete cover were not available from the paper of
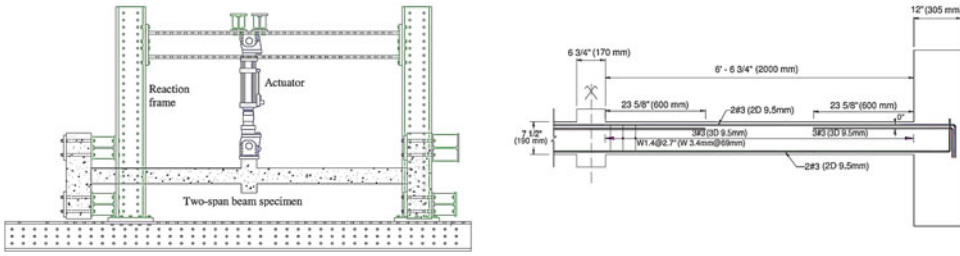
**Figure 14.** Specimen setup and reinforcement detail (Sasani, Werner, and Kazemi 2011).
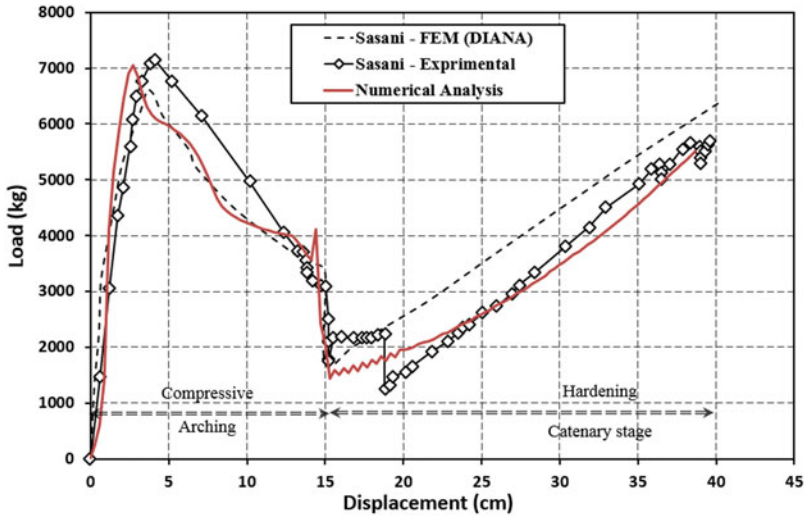


**Figure 15.** Load-displacement responses for Sasani et al.'s frame.

Sasani, Werner, and Kazemi (2011), a section width of 168 mm and a cover of 20 mm have been assumed in the simulation (For more details, see Sasani, Werner, and Kazemi (2011)). According to material properties, the concrete tension strength is assumed about 0.36 ksi (2.5 MPa) with strain cracking at the peak tensile stress of about 0.00015. Also, the confining effect of transverse reinforcement on the concrete compressive strength and stiffness is also taken into account using proposed model by Ghorbi, Soltani, and Maekawa (2013). The number of sub-step increments is considered 130 steps with the initial displacement increment of 3 mm in each applied load factor.

It is observed that the value of the ultimate load predicted by the presented approach $P = 7056$ kg (at vertical displacement of 30 mm) correlates relatively well with the experimental result of $P = 7143$ kg (at vertical displacement of 40 mm). Moreover, according to reported experimental observations, at vertical displacements of about 190 mm, the two bottom bars fractured which are equal to the beam section's depth.

As can be inferred in Fig. 15 and experimental observations, following the bar fracture, catenary action provided by the top reinforcement results in increased resistance of the beam in a column collapse scenario. At a vertical displacement of about 190 mm, the top continuous bars at the center of the beam, which were previously in compression, yielded in tension. The tensile strain in these bars increased to about 0.05 at a maximum vertical displacement of about 400 mm. Therefore, the post-peak response obtained from the presented methodology correlates relatively well with that of the experiment and captures the arch-action and membrane action of the member quite accurately.
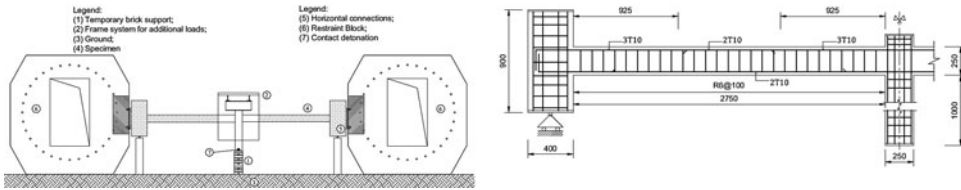
**Figure 16.** Specimen setup and reinforcement detail (Pham, Tan, and Yu 2017).
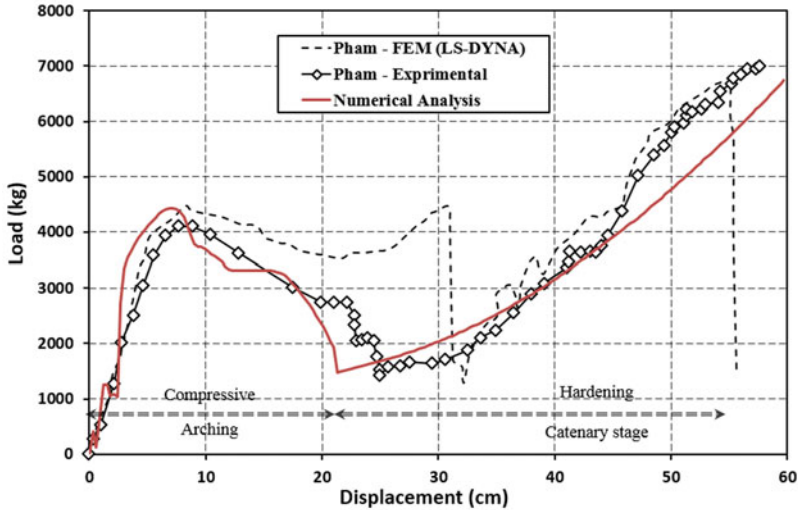


**Figure 17.** Load-displacement responses for Pham et al.'s frame.

Another quasi-static verification was conducted by Pham et al. at Nanyang technological university which is chosen to investigate membrane action behavior in RC elements (Fig. 16). The test series included eight specimens with the same geometry and different reinforcement ratios and arrangement (six specimens) and different beam-spans (two specimens). For more details of rebar detailing and material properties of all specimens refer to Pham, Tan, and Yu (2017).

It is observed that the value of the ultimate load predicted by the presented approach to be about $P = 4300$ kg (at vertical displacement of 79 mm) correlates relatively well with the experimental result (Specimen S1) of $P = 4100$ kg (at vertical displacement of 85 mm). As can be inferred from results of presented methodology, the membrane segment of response is obtained underestimation relative to experimental test due to some assumption of analysis which was not available in Pham et al.'s paper such as concrete cover and ultimate strength of bars.

The equilibrium path was constructed by 50-100 unequal steps and an absolute norm of displacement with a 0.001 convergence tolerance was adopted. The number of iterations required for convergence criteria varied from 10 to 20 at different displacement step levels. Moreover, the longitudinal strain profile of concrete and fiber sets are demonstrated, respectively. Both experimental tests are simulated as Fig. 18a and strain distributions correspond to the maximum vertical resisting force at the vertical displacement of 30 mm (for Sasani et al.'s test) and 79 mm (for Pham et al.'s test) as Fig. 18b obtained from fibers with red colors. Note that the bars did not fracture together during the experiment due to lack of complete symmetry in geometry and material properties, while the simulation is completely symmetric and the bars fracture simultaneously in the present model.
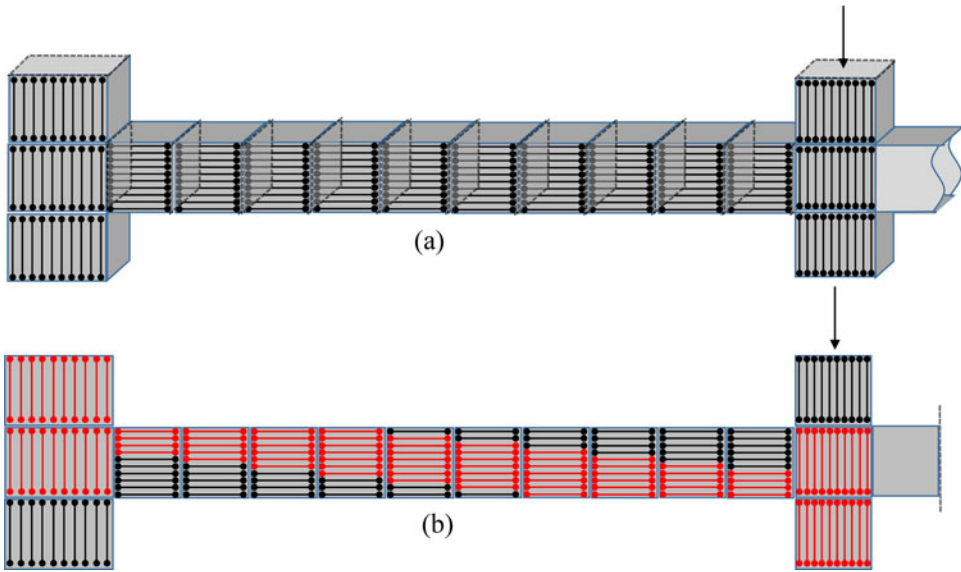
**Figure 18.** (a) Fiber sets among interface elements, (b) Strain variation at the vicinity of the removed column at the peak vertical resisting force.

## 8. Conclusions

This paper studied the membrane action behavior of RC structural members according to the scenario of a potential progressive collapse of structures as a result of the removal of a load-bearing element. For this purpose, a two-stage fibers based method was proposed in a Lagrangian description. Its first stage dealt with the compressive arch action by the updated Lagrangian formulation. In this stage, the probable shear deformation and bond-slip effect were implicitly included. Moreover, the first stage assembled a displacement-based interface and Timoshenko fiber planar elements in order to consider the nonlinear flexural-shear interactions and local stress-strain behaviors in RC members. In the second stage, the total Lagrangian approach was developed to express the catenary stages in the large displacement cases and the effect of second order strain terms is considered in the formulation of this stage. The suggested method is capable of taking into account both geometric and material nonlinearity. Additionally, it can be easily applied in practical engineering problems. The numerical results showed that the development of catenary action could be investigated through two separate stages of resisting mechanisms: compressive arc action and catenary action with flexure and shear interaction. It is worthwhile to highlight that the capability and accuracy of the suggested formulation were assessed by comparing the obtained results with those of other researchers' experimental and numerical ones. The comparison shows that the proposed method can yield relatively accurate and convergent results in dealing with the problems, and the formulation has the potential to be employed for simulating multi-storey RC frames subjected to large deformations.

## Acknowledgments

## ORCID

Behrooz Yousefi http://orcid.org/0000-0002-4792-5890
Mohammad Reza Esfahani http://orcid.org/0000-0002-2655-2466

## References

Alemdar, Bulent N., and Donald W. White. 2005. Displacement, flexibility, and mixed beam–column finite element formulations for distributed plasticity analysis. *Journal of Structural Engineering* 131 (12):1811–19. doi:10.1061/(ASCE)0733-9445(2005)131:12(1811).

Bao, Yihai, Hai S. Lew, and Sashi K. Kunnath. 2014. Modeling of reinforced concrete assemblies under column-removal scenario. *Journal of Structural Engineering* 140 (1):04013026. doi:10.1061/(ASCE)ST.1943-541X.0000773.

Bathe, Klaus-Jürgen, and Said Bolourchi. 1979. Large displacement analysis of three-dimensional beam structures. *International Journal for Numerical Methods in Engineering* 14 (7):961–86. doi:10.1002/nme.1620140703.

Bazoune, A., YA. Khulief, and NG. Stephen. 2003. Shape functions of three-dimensional Timoshenko beam element. *Journal of Sound and Vibration* 259 (2):473–80. doi:10.1006/jsvi.2002.5122.

Ben-Dor, G., A. Dubinsky, and T. Elperin. 2009. Optimization of reinforced concrete panels with rear face steel liner under impact loading. *Mechanics Based Design of Structures and Machines* 37 (4):503–12. doi:10.1080/15397730903190438.

Bocciarelli, Massimiliano, and Gaia Barbieri. 2017. A numerical procedure for the pushover analysis of masonry towers. *Soil Dynamics and Earthquake Engineering* 93:162–71. doi:10.1016/j.soildyn.2016.07.022.

Brunesi, E., and R. Nascimbene. 2014. Extreme response of reinforced concrete buildings through fiber force-based finite element analysis. *Engineering Structures* 69:206–15. doi:10.1016/j.engstruct.2014.03.020.

Brunesi, E., R. Nascimbene, F. Parisi, and N. Augenti. 2015. Progressive collapse fragility of reinforced concrete framed structures through incremental dynamic analysis. *Engineering Structures* 104:65–79. doi:10.1016/j.engstruct.2015.09.024.

Brunesi, Emanuele, and Fulvio Parisi. 2017. Progressive collapse fragility models of European reinforced concrete framed buildings based on pushdown analysis. *Engineering Structures* 152:579–96. doi:10.1016/j.engstruct.2017.09.043.

Chun, Sung-Chul, and Dae-Young Kim. 2004. Evaluation of mechanical anchorage of reinforcement by exterior beam-column joint experiments. Paper read at Proceedings of 13th World Conference on Earthquake Engineering.

Collins, MP., Frank J. Vecchio, and G. Mehlhorn. 1985. An international competition to predict the response of reinforced concrete panels. *Canadian Journal of Civil Engineering* 12 (3):624–44. doi:10.1139/l85-070.

Crivelli, Luis A., and Carlos A. Felippa. 1993. A three-dimensional non-linear Timoshenko beam based on the core-congruential formulation. *International Journal for Numerical Methods in Engineering* 36 (21):3647–73. doi:10.1002/nme.1620362106.

De Souza, Remo Magalhães. 2000. *Force-based finite element for large displacement inelastic analysis of frames.* Berkeley California: University of California.

Deluce, Jordon Robert. 2011. *Cracking behaviour of steel fibre reinforced concrete containing conventional steel reinforcement, civil engineering department.* Toronto: University of Toronto.

Dong, SB., C. Alpdogan, and E. Taciroglu. 2010. Much ado about shear correction factors in Timoshenko beam theory. *International Journal of Solids and Structures* 47 (13):1651–65. doi:10.1016/j.ijsolstr.2010.02.018.

Dvorkin, Eduardo N., Eugenio Onte, and Javier Oliver. 1988. On a non-linear formulation for curved Timoshenko beam elements considering large displacement/rotation increments. *International Journal for Numerical Methods in Engineering* 26 (7):1597–613. doi:10.1002/nme.1620260710.

Felippa, Carlos A. 2001. *Nonlinear finite element methods, University of Colorado., Boulder, Colorado, USA*: Department of Aerospace Engineering Sciences and Center for Space Structures and Controls.

Felippa, Carlos A., and Bjorn Haugen. 2005. A unified formulation of small-strain corotational finite elements: I. Theory. *Computer Methods in Applied Mechanics and Engineering* 194 (21-24):2285–335. doi:10.1016/j.cma.2004.07.035.

Feng, Decheng, Chinmoy Kolay, James M. Ricles, and Jie Li. 2016. Collapse simulation of reinforced concrete frame structures. *The Structural Design of Tall and Special Buildings* 25 (12):578–601. doi:10.1002/tal.1273.

Feng, YT., D. Perić, and DRJ. Owen. 1995. Determination of travel directions in path-following methods. *Mathematical and Computer Modelling* 21 (7):43–59. doi:10.1016/0895-7177(95)00030-6.

Franchi, Alberto, DE. Grierson, and MZ. Cohn. 1981. A computer system for the elastic-plastic analysis of large-scale structures. *Journal of Structural Mechanics* 9 (3):295–324. doi:10.1080/03601218108907389.

Gerasimidis, Simos, George Deodatis, Thalia Kontoroupi, and Mohammed Ettouney. 2015. Loss-of-stability induced progressive collapse modes in 3D steel moment frames. *Structure and Infrastructure Engineering* 11 (3):334–44. doi:10.1080/15732479.2014.885063.

Ghaisas, Kunal V., Dhiman Basu, Svetlana Brzev, and Juan José Pérez Gavilán. 2017. Strut-and-Tie Model for seismic design of confined masonry buildings. *Construction and Building Materials* 147:677–700. doi:10.1016/j.conbuildmat.2017.04.200.

Gharib, Mohammad Reza, Seyyed Amirreza Vaziri, and Ramin Memarbashi. 2019. Experimental and numerical investigation of concrete properties effects on fracture toughness under complex loading. *Mechanics Based Design of Structures and Machines*:1. doi:10.1080/15397734.2019.1619580.

Ghorbi, Ehsan, Masoud Soltani, and Koichi Maekawa. 2013. Development of a compressive constitutive model for FRP-confined concrete elements. *Composites Part B: Engineering* 45 (1):504–17. doi:10.1016/j.compositesb.2012.07.014.

Goodman, Richard E., Robert L. Taylor, and Tor L. Brekke. 1968. A model for the mechanics of jointed rock. *Journal of Soil Mechanics & Foundations Div* 94:637–59.

Herrmann, Leonard R. 1978. Finite element analysis of contact problems. *Journal of the Engineering Mechanics Division No* 104 (5):1043–57.

Izzuddin, BA., AG. Vlassis, AY. Elghazouli, and DA. Nethercot. 2008. Progressive collapse of multi-storey buildings due to sudden column loss—Part I: Simplified assessment framework. *Engineering Structures* 30 (5):1308–18. doi:10.1016/j.engstruct.2007.07.011.

Jirásek, Milan, and Zdenek P. Bazant. 2002. *Inelastic analysis of structures*. New Jersey: John Wiley & Sons.

Kabeyasawa, Toshimi, Hitoshi Shiohara, Shunsuke Otani, and Hiroyuki Aoyama. 1983. Analysis of the full-scale seven-story reinforced concrete test structure. *Journal of the Faculty of Engineering, University of Tokyo No* 37 (2):431–78.

Kaewkulchai, Griengsak, and Eric B. Williamson. 2004. Beam element formulation and solution procedure for dynamic progressive collapse analysis. *Computers & Structures* 82 (7-8):639–51. doi:10.1016/j.compstruc.2003.12.001.

Kara, Ilker Fatih, and Cengiz Dundar. 2010. Three-Dimensional Analysis of Tall Reinforced Concrete Buildings with Nonlinear Cracking Effects#. *Mechanics Based Design of Structures and Machines* 38 (3):388–402. doi:10.1080/15397734.2010.483551.

Li, Baolu. 1989. Contact density model for stress transfer across cracks in concrete. *Journal of the Faculty of Engineering, the University of Tokyo* (1):9–52.

Li, Yi, Xinzheng Lu, Hong Guan, and Lieping Ye. 2011. An improved tie force method for progressive collapse resistance design of reinforced concrete frame structures. *Engineering Structures* 33 (10):2931–42. doi:10.1016/j.engstruct.2011.06.017.

Li, Yi, Xinzheng Lu, Hong Guan, and Lieping Ye. 2014. Progressive collapse resistance demand of reinforced concrete frames under catenary mechanism. *ACI Structural Journal* 111 (5). doi:10.14359/51686809.

Limkatanyu, Suchart, Woraphot Prachasaree, Griengsak Kaewkulchai, and Enrico Spacone. 2014. Unification of mixed Euler-Bernoulli-Von Karman planar frame model and corotational approach. *Mechanics Based Design of Structures and Machines* 42 (4):419–41. doi:10.1080/15397734.2013.879042.

Lodygowski, Tomasz, and Maciej Szumigala. 1992. Engineering models for numerical analysis of composite bending members. Mechanics of Structures *and Machines* 20 (3):363–80. doi:10.1080/08905459208905173.

Maekawa, Koichi, Hajime, Okamur, and Amorn Pimanmas. 2003. *Non-linear mechanics of reinforced concrete*. London: Spon Press.

Neuenhofer, Ansgar, and Filip C. Filippou. 1998. Geometrically nonlinear flexibility-based frame finite element. *Journal of Structural Engineering* 124 (6):704–11. doi:10.1061/(ASCE)0733-9445(1998)124:6(704).

Noghabai, Keivan. 2000. Behavior of tie elements of plain and fibrous concrete and varying cross sections. *Structural Journal* 97 (2):277–84.

Oehlers, Deric John, IST. Liu, and R. Seracino. 2005. The gradual formation of hinges throughout reinforced concrete beams. *Mechanics Based Design of Structures and Machines* 33 (3-4):373–98. doi:10.1080/15367730500458234.

Okamura, H., and K. Maekawa. 1991. *Nonlinear analysis and constitutive models of reinforced concrete*. Tokyo: Gihodo-Shuppan Co.

Orakcal, Kutay, Leonardo Maximiliano Massone Sanchez, and John W. Wallace. 2006. *Analytical modeling of reinforced concrete walls for predicting flexural and coupled-shear-flexural responses*. California, Berkeley: Pacific Earthquake Engineering Research Center, College of Engineering, University of California, Berkeley.

Palermo, Daniel, and Frank J. Vecchio. 2003. Compression field modeling of reinforced concrete subjected to reversed loading: Formulation. *ACI Structural Journal* 100 (5):616–25.

Pang, Xiao-Bo David, and Thomas TC. Hsu. 1995. Behavior of reinforced concrete membrane elements in shear. *Structural Journal* 92 (6):665–79.

Parisi, Fulvio, and Nicola Augenti. 2012. Influence of seismic design criteria on blast resistance of RC framed buildings: A case study. *Engineering Structures* 44:78–93. doi:10.1016/j.engstruct.2012.05.046.

Pham, Anh Tuan, Kang Hai Tan, and Jun Yu. 2017. Numerical investigations on static and dynamic responses of reinforced concrete sub-assemblages under progressive collapse. *Engineering Structures* 149:2–20. doi:10.1016/j.engstruct.2016.07.042.

Qureshi, J. 1933. Computational model for steel bar embedded in concrete under combined axial pullout and transverse shear displacement. *Proc. of JCI* 15 (2):1249–54.

Sasani, Mehrdad, Andre Werner, and Ali Kazemi. 2011. Bar fracture modeling in progressive collapse analysis of reinforced concrete structures. *Engineering Structures* 33 (2):401–409. doi:10.1016/j.engstruct.2010.10.023.

Schweizerhof, KH., and P. Wriggers. 1986. Consistent linearization for path following methods in nonlinear FE analysis. *Computer Methods in Applied Mechanics and Engineering* 59 (3):261–79. doi:10.1016/0045-7825(86)90001-0.

Shima, Hiroshi, Lie-Liung Chou, and Hajime Okamura. 1987. Micro and macro models for bond in reinforced concrete. *Journal of the Faculty of Engineering* 39 (2):133–94.

Soltani, Masoud, Xuehui An, and Koichi Maekawa. 2003. Computational model for post cracking analysis of RC membrane elements based on local stress–strain characteristics. *Engineering Structures* 25 (8):993–1007. doi:10.1016/S0141-0296(03)00042-7.

Soltani, Masoud, Xuehui An, and Koichi Maekawa. 2005. Localized nonlinearity and size-dependent mechanics of in-plane RC element in shear. *Engineering Structures* 27 (6):891–908. doi:10.1016/j.engstruct.2005.01.011.

Tsai, Meng-Hao, and Bing-Hui Lin. 2008. Investigation of progressive collapse resistance and inelastic response for an earthquake-resistant RC building subjected to column failure. *Engineering Structures* 30 (12):3619–28. doi:10.1016/j.engstruct.2008.05.031.

Valipour, Hamid R., and Stephen J. Foster. 2010. Finite element modelling of reinforced concrete framed structures including catenary action. *Computers & Structures* 88 (9-10):529–38. doi:10.1016/j.compstruc.2010.01.002.

Vecchio, Frank J., and Michael P. Collins. 1986. The modified compression-field theory for reinforced concrete elements subjected to shear. *Journal of the American Concrete Institute* 83 (2):219–31.

Vlassis, AG., BA. Izzuddin, AY. Elghazouli, and DA. Nethercot. 2008. Progressive collapse of multi-storey buildings due to sudden column loss—Part II: Application. *Engineering Structures* 30 (5):1424–38. doi:10.1016/j.engstruct.2007.08.011.

Williams, FW. 1964. An approach to the non-linear behaviour of the members of a rigid jointed plane framework with finite deflections. *The Quarterly Journal of Mechanics and Applied Mathematics* 17 (4):451–69. doi:10.1093/qjmam/17.4.451.

Wu, YF., DJ. Oehlers, and MC. Griffith. 2002. Partial-interaction analysis of composite beam/column members. *Mechanics of Structures and Machines* 30 (3):309–32. doi:10.1081/SME-120004420.

Yousefi, Behrooz, Mohammad Reza Esfahani, and Mohammadreza Tavakkolizadeh. 2018. A mixed finite element formulation for Timoshenko fiber models based on the local stress field. Paper read at JVE International Ltd. *Vibroengineering Procedia.* doi:10.21595/vp.2018.19808.

Yu, Jun, and Kang Hai Tan. 2014. Analytical model for the capacity of compressive arch action of reinforced concrete sub-assemblages 4:109–26.

Yu, Xiao Hui., Da Gang Lu, Kai Qian, and Bing Li. 2017. Uncertainty and sensitivity analysis of reinforced concrete frame structures subjected to column loss. *Journal of Performance of Constructed Facilities* 31 (1):04016069. doi:10.1061/(ASCE)CF.1943-5509.0000930.

Zhai, Ximei, Yonghui Wang, and Zhenyu Sun. 2019. Damage model and damage assessment for single-layer reticulated domes under exterior blast load. *Mechanics Based Design of Structures and Machines* 47 (3):319–38. doi:10.1080/15397734.2018.1549496.

Zhang, Fuwen, Xilin Lu, and Chao Yin. 2009. Numerical simulation and analysis for collapse responses of RC frame structures under earthquake. *Frontiers of Architecture and Civil Engineering in China* 3 (4):364. doi:10.1007/s11709-009-0061-y.